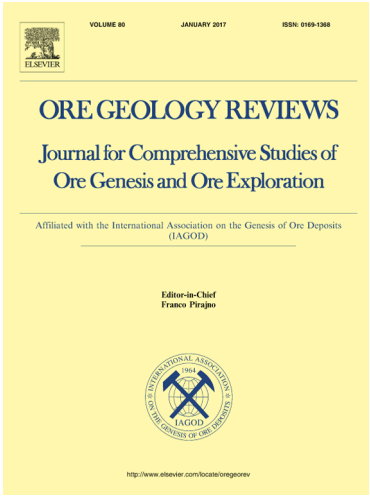

U-Pb SIMS and Ar-Ar geochronology, petrography, mineralogy and gold mineralization of the late Mesozoic Amga alkaline rocks (Aldan shield, Russia)

I.R. Prokopyev, A.G. Doroshkevich, A.V. Ponomarchuk, A.A. Redina, I.V. Yegitova, J.D. Ponomarev, S.A. Sergeev, A.A. Kravchenko, A.I. Ivanov, E.P. Sokolov, E.A. Kardash, A.V. Minakov

PII: S0169-1368(18)30691-7
DOI: https://doi.org/10.1016/j.oregeorev.2019.05.011
Reference: OREGEO 2925

To appear in: *Ore Geology Reviews*

Received Date: 13 August 2018
Revised Date: 30 April 2019
Accepted Date: 10 May 2019

Please cite this article as: I.R. Prokopyev, A.G. Doroshkevich, A.V. Ponomarchuk, A.A. Redina, I.V. Yegitova, J.D. Ponomarev, S.A. Sergeev, A.A. Kravchenko, A.I. Ivanov, E.P. Sokolov, E.A. Kardash, A.V. Minakov, U-Pb SIMS and Ar-Ar geochronology, petrography, mineralogy and gold mineralization of the late Mesozoic Amga alkaline rocks (Aldan shield, Russia), *Ore Geology Reviews* (2019), doi: https://doi.org/10.1016/j.oregeorev.2019.05.011

U-Pb SIMS and Ar-Ar geochronology, petrography, mineralogy and gold mineralization of the late Mesozoic Amga alkaline rocks (Aldan shield, Russia)

Prokopyev I.R.[a,b*], Doroshkevich A.G.[a,c,d], Ponomarchuk A.V.[a], Redina A.A.[a], Yegitova I.V.[a,b], Ponomarev J.D.[a,b], Sergeev S.A.[e], Kravchenko A.A.[f,g], Ivanov A.I.[f], Sokolov E.P.[h], Kardash E.A.[h], Minakov A.V.[h]

a – Sobolev Institute of Geology and Mineralogy, Siberian Branch of the Russian Academy of Sciences, pr. Akademika Koptyuga 3, 630090, Novosibirsk, Russia

b – Novosibirsk State University, st. Pirogova 2, 630090, Novosibirsk, Russia

c – Tomsk State University, Lenin Ave. 36, 634050, Tomsk, Russia

d – Geological Institute, Siberian Branch of the Russian Academy of Sciences, st. Sakhyanova 6a, 670047, Ulan-Ude, Russia

e – AP Karpinsky Russian Geological Research Institute, pr. Sredny 74, 199106, St. Petersburg,

f – Russian Institute of Diamond and Precious Metal Geology, Siberian Branch, Russian Academy of Sciences, st. Lenina 39, 677980, Yakutsk, Russia

g – Ammosov Northeastern Federal University, st. Belinskogo 58, 677000, Yakutsk, Russia

h – "Yakutskgeologiya" Federal State Unitary Mining Geological Enterprise of the Sakha Republic, st. Kalvica 24, 677009, Yakutsk; Aldan Branch, st. Lenina 8, 678900, Aldan, Russia

*** –** Corresponding author: Dr. Prokopyev Ilya, e-mail addresses: prokopev_ilya@mail.ru prokop@igm.nsc.ru

Abstract

Late Mesozoic Upper Amga alkaline rocks are located in the Amga tectonic mélange zone within the Aldan-Stanovoy shield, Russia. The main phases of the Upper Amga complex consist of alkaline syenite intrusions as well as the lamprophyre dikes and sills. The mineralogical features indicate that the lamprophyre may belong to minette. Recent geological works revealed the linear and area-specific geochemical gold anomalies in association with late Mesozoic alkaline magmatism in the Upper Amga gold district. The age of the syenite intrusions is 131.4 ± 1.5 (2.9) Ma, and the lamprophyre sills and dikes were formed at 134.9 ± 1.6, 132.3 ± 1.5 and 117.7 ± 3.4 Ma. The mineralization is represented by the REE-Ti-Th, polymetallic (sulfide) and telluride-gold types in the quartz-calcite-chlorite alteration of the main magmatic phases of the alkaline rocks. The fluid inclusions study shows that the sulfides were formed from hydrothermal fluids of CO_2-N_2-NaCl-H_2O composition at temperatures ranging from 390 to 340°C, with 44-22.7 wt.% NaCl-eq, whereas the epithermal telluride-gold mineralization originated

from low-temperature CO_2±N_2-NaCl-H_2O fluids, with the homogenization temperature of 230-210°C and a of 9.2-3.3 wt.% NaCl-eq.

Key words

Aldan-Stanovoy shield, late Mesozoic, alkaline magmatism, alkaline syenite, lamprophyre, gold, fluid inclusion study.

1. Introduction

The Aldan-Stanovoy shield contains gold, uranium, molybdenum and platinum (PGE) deposits in association with the late Mesozoic alkaline magmatic complexes, e.g., Kuranakh, Ryabinovoe, Samolazovskoe, Lebedinoe, Inagli (Bilibin, 1959; Kazansky, 2004; Kochetkov, 2006; Maximov, 2003; Maximov et al., 2010; Vetluzhskikh, 2002). The first report on gold in the Aldan district dates back to 1899, with a discovery of economically viable gold by MP Tarabukin and VP Bertin in 1924 (Khatylaev, 1972). Today, Aldan is a major mining district in the Russian Far East, with an estimated total historical gold production of 540 tonnes (including of 250 tonnes of gold from the Kuranakh deposit) (Goryachev and Pirajno, 2014). The Chara-Aldan metallogenic province is located in the Aldan-Stanovoy shield (Dzevanovskii et al., 1972; Vetluzhskikh, 1990; Maximov, 2003). This zone consists of several local mineral districts (Upper Amga, Central Aldan, Tyrkanda and Ket-Kap), in which gold deposit and occurrences associate with the late Mesozoic alkaline magmatism.

The late Mesozoic ore-magmatic systems within the Siberian craton and adjacent regions were formed against the background of the assembly and breakup of supercontinents (Goldfarb et al., 2014; Goryachev and Pirajno, 2014; Guo et al., 2013; Pirajno and Santosh, 2014; Zhai and Santosh, 2013). According to Yarmolyuk et al. (1995, 2000), the Mesozoic igneous activity in the Siberian craton was generated by the sublithospheric "mantle hot field" expressed in intense rifting and intraplate volcanoplutonic activity, accompanied by epicontinental basins and grabens. According to Khomich et al. (2014, 2015), dehydration of the subducting oceanic slab and subsequent upwelling of the asthenospheric mantle was responsible for generation of the ore-forming fluids and formation of the gold, uranium and PGE deposits.

The late Mesozoic alkaline complexes of the Central-Aldan district are predominantly represented by monzonite, syenite, leucite syenite, lamprophyre, alkaline mafic and granite-granodiorite rocks, with their ages ranging from 160 to 115 Ma (Borisenko et al., 2011; Dvornik, 2009; Kazansky, 2004; Kochetkov, 2006; Maximov, 2003; Maximov et al., 2010; Prokopyev et al., 2018). The Upper Amga gold district has been relatively poorly studied because of limited access. Until recently, only alluvial gold placers were worked in this region. During 2012-13, Yakutskgeologiya conducted advanced geological, geophysical and geochemical works and identified linear geochemical gold anomalies in association with the late Mesozoic syenite magmatism (Sokolov, 2015). The anomalies correspond to

gold-sulfide-bearing hydrothermal alteration. Syenite rocks were preliminary dated at 140 ± 7 Ma (Rb-Sr method; Anisimova et al., 2016).

In this paper, we present new geochronological, petrographic and mineralogical data for the main magmatic phases of the late Mesozoic Upper Amga alkaline rocks and constrain the mineral composition and fluid regime for the formation of gold mineralization. Location of the Upper Amga district within the Amga tectonic mélange zone undoubtedly reflects the specific features of the late Mesozoic alkaline magmatic rocks.

2. Analytical methods

A representative set of samples of the Upper Amga alkaline magmatic rocks and hydrothermal alteration was collected by the authors in 2016-17, with some samples provided by Yakutskgeologiya exploration company. The rock material originated from drill core and trenches.

The mineral composition of the rocks was determined using the scanning electron microscope TESCAN MIRA 3 LMU JSM-6510LV with energy-prefix X-Max Oxford Instruments and the electron microprobe JEOL JXA-8100 (WDS mode, 20 kV, 15 nA, 1–2 μm beam diameter). Accumulation time for analyzing of F (using LDE crystal) was 40 s (20 s – counting of background; 20 s – counting of peak for F), detection limit for F was 477 ppm (0.04 wt.%). For silicate minerals, we used a beam current of 10 nA and an acceleration voltage of 15 kV; for Fe-Ti oxides 20 nA and 15 kV, for monazite 40 nA and 20 kV, for apatite 10 nA and 20 kV. The peak counting time was 16 s for major elements and 30-60 s for minor elements. For calibration, both natural minerals and synthetic phases were used as standards (Lavrent'ev et al., 2015). For Au-Ag alloys and Au-Pb-Te compounds, the standards used were: $Au_{75}Ag_{25}$ (Au*M*α; Ag*L*α), Cu-met (CuKα), HgTe (Hg*M*β), PbTe (Pb*M*α), and Sb_2S_3 (Sb*L*α). The detection limits for individual elements were: 0.07 wt.% for Au, 0.07 wt.% for Ag, 0.06 wt.% for Cu, 0.07 wt.% for Hg, 0.04 wt.% for Pb, and 0.08 wt.% for Sb. For Pb-Au-Fe-Ca-Al-Si compounds, the standards used were: O-145 (pyrope) (Fe*K*α; Al*K*α; Si*K*α; Ca*K*α), PbS (Pb*M*α), $Au_{75}Ag_{25}$ (Au*M*α; Ag*L*α), ZnS (Zn*K*α), IGEM (Mn garnet) (Mn*K*α), and GL-6 (glass) (Ti*K*α). Estimated detection limits were: 0.02 wt.% for Fe, 0.01 wt.% for Al, 0.01 wt.% for Si, 0.035 wt.% for Pb, 0.03 wt.% for Au, 0.04 wt.% for Ag, 0.03 wt.% for Zn, 0.02 wt.% for Mn, 0.01 wt.% for Ca, 0.01 wt.% for Ti.

Double-polished thin sections were prepared for fluid inclusion investigations. Raman spectroscopy was applied to determine the composition of gas and crystalline solid phases of fluid inclusions. Raman spectra were obtained on a LabRam HR800 Horiba Jobin Yvon spectrometer, equipped with an optical microscope (Olympus BX41). The 514.5 nm Ar + laser line was used for spectra excitation. Heating and freezing experiments were carried out using Linkam THMSG-600 stage with a measuring range from -196 to +600°C, and include the determination of homogenization temperatures and salt composition of fluid inclusions. The accuracy of measurements in the temperature interval from -20 to +80°C is ± 0.1°C, and beyond this interval, it was ± 1°C. The salt concentration of crystal-fluid inclusions was determined using NaCl-H_2O diagram, and was calculated from the melting point of the

salt crystals (Roedder, 1984; Bodnar and Vityk, 1994). Composition and concentration of gas-liquid fluid inclusion solution were identified using eutectic and ice melting temperatures according to the data listed in Borisenko (1977) and (Bodnar and Vityk, 1994).

The $^{40}Ar/^{39}Ar$ dating was performed on monomineralic fractions by stepwise heating (Travin et al., 2009). The mineral grains were placed into an Al-foil package and stacked in a silica tube. Irradiation was performed in the Cd and B_2C_3-plated channel of the RBT-10/2 reactor (GSC SRIAR, mitrovograd, Russia). For calibration we used the international standard biotite (Lp-6) and muscovite (Bern 4 m) (Baksi et al., 1996). The Ar isotope composition was measured on a Noble Gas 5400 mass spectrometer with measurement errors within ± 1r. Additional purification of Ar was carried in Zr and Ti-Al SAES getters and in appendix, cooling by liquid nitrogen. The temperature in the reactor was monitored by Al-thermocouple.

Zircon crystals were mounted in epoxy along with grains of the TEMORA and 91500 zircon standards. The microanalysis points were selected with the help of optical, BSE, and cathodoluminescence images, which showed the internal structure and zoning of the zircon crystals. The U-Pb ratios were measured using the method recommended by Williams (1998). The intensity of the primary beam of molecular oxygen was 4 nA, and the crater created was 25 μm in diameter and up to 5 μm deep. The data were processed with SQUID software (Ludwig, 2000). The U-Pb ratios were normalized to the value 0.0668 (TEMORA), which corresponds to 416.75 Ma (Black et al., 2003). Individual analyses are within 1σ error, and the calculated concordant ages are within 2σ error. The concordia diagrams were plotted with Isoplot/Ex software (Ludwig, 1999).

Mineralogical, geochemical and fluid inclusion investigations and Ar-Ar dating were carried out at the Analytical Center for Multi-Elemental and Isotope Research, Siberian Branch of the Russian Academy of Sciences (Novosibirsk, Russia). Zircon dating using the U-Pb SIMS method was carried out on a SHRIMP II at the Centre for Isotopic Research, Karpinsky Geological Research Institute (VSEGEI), St.-Petersburg, Russia.

3. Geological background

The Upper Amga gold district in southern Yakutia (Sakha Republic) occurs approximately 120 km to the west of the town of Aldan, in the upper reaches of the Amga River (the tributary of the Aldan River). This territory is difficult to access (Fig. 1).

According to the available data, the Aldan-Stanovoy shield comprises five superterranes (Parfenov and Kuzmin, 2001), which are separated by the tectonic mélange zones (Fig. 1a): West Aldan (WA) superterrane; Nimnyr (ANM) and Sutam (AST) terranes in the Central Aldan superterrane; Batomga (EBT) and Uchur (EUC) terranes, making up the East Aldan superterrane; Tynda (TN) and Chogar (CG) superterranes.

The Upper Amga gold district coincides with the Amga tectonic mélange zone (Fig. 1a). It separates the Central Aldan superterrane from the West Aldan and Tynda terranes to the west and south,

respectively, and cuts off the Kalar tectonic mélange zone. The Amga zone is arcuate in plan view, extending for 650 km, with a width ranging from a few kilometres to 150 km. The structural pattern of the zone is defined by numerous thrusts, strike-slip faults and associated folds, oriented along the strike of the zone (Parfenov and Kuzmin, 2001; Sal'nikova, 1993). The basement lithologies differ significantly in composition, age, and metamorphic grade. The most widespread is the granite-gneisses, while tonalite-trondhjemite gneiss is subordinate. Also present are the paragneisses, which are fragments of the greenstone belts of Archean and Paleoproterozoic ages, saturated with differentiated plutons of gabbro-diorite-plagiogranite composition (Kotov, 2003; Kotov et al., 1995, 2004a,b, 2005; Parfenov and Kuzmin, 2001; Sal'nikova et al., 1997; Velikoslavinskii et al., 2011).

The structural position of the Upper Amga district is characterized by: an early Precambrian basement, a Vendian to Lowwer Cambrian sedimentary basin, and Mesozoic orogenic activity (Fig. 1b). Archean basement rocks are unconformably overlain by the Vendian to Lower Cambrian marine clay-carbonate rocks. In some areas Jurassic to Cenozoic clastic sequences are locally preserved.

The tectonic pattern of the Upper Amga district is controlled by the north-south-striking Amga regional fault (Fig. 1), which was repeatedly reactivated, especially during the Mesozoic, when magmatism and associated hydrothermal activity were intensively developed. There are four varieties of the late Mesozoic alkaline intrusions in the Upper Amga ore province (Fig. 1b): (1) dikes and stocks of mafic and ultramafic alkaline rocks (shonkinite, pyroxenite and syenite-porphyry); (2) stocks, laccoliths and sills of alkaline syenites, syenite-porphyries, and monzonites; (3) lamprophyre sills and dikes; and (4) aegirine granite stocks. The alkaline syenite and lamprophyre intrusions occur in zones of sulfidization, silicification, carbonatization and chloritization, accompanied by gold mineralization.

4. Geochronology

The previous Rb-Sr data on the alkaline rocks of the Upper Amga district yielded an age of 140 ± 7 Ma (Anisimova et al., 2016). The Ar-Ar ages of the phlogopites from the syenite (sample No. 16081) and from the lamprophyre dike (No. 13070) are 129.1 ± 2.5 and 117.7 ± 3.4 Ma, respectively (Fig. 1b, Ponomarchuk et al., 2019a). For the SIMS U-Pb dating, we used the zircons from the syenite sample No. 16081; and for the Ar-Ar analyses, we used the K-feldspar from the syenite sample No. 5088, the phlogopite from the lamprophyre sill sample No. 9106 and K-feldspar from the lamprophyre dike sample No. 17086, all selected from the northwestern part of the Upper Amga district (Fig. 1b).

Zircon is an accessory mineral of the syenites, which forms rare crystals and detrital grains, up to 0.3 mm in size in the rock matrix (Fig. 2a). The crystals combine bipyramidal and prismatic habits, and the grains have usually two- or three-phase structures in the cathodoluminescence (CL) images. These zircons show the clear metamict domains with microfractures, which are reflected in the analytical data. Some zircons have dark cores with indistinct oscillatory zoning in the rims in the CL image, and the Th/U values vary from 0.3 to 1.06 (Table 1).

The U-Pb SIMS zircon dating shows the three clusters of the Concordia dates corresponding to the intervals of 2.5-2.2, 1.9-1.87 Ga and 130 Ma (Fig. 2b). The Late Mesozoic interval determines the age of the syenite crystallization of 131.4 ± 2.9 Ma (according to the three diagnostic points, Fig. 2c), and the age coincides with the previously obtained Ar-Ar geochronological data of 129.1 ± 2.5 Ma (sample No. 16081, Ponomarchuk et al., 2019a).

The $^{40}Ar/^{39}Ar$ age spectrum for the K-feldspar from the syenite sample No. 5088 (Fig. 1b) shows an age plateau of 131.4 ± 1.5 Ma, which corresponds to approximately 63% of the cumulative ^{39}Ar (Fig. 3a, Table 2). The age of the syenite sample No. 5088 correlates with the previous Ar-Ar and the present U-Pb data of the age characteristics of the syenite sample No. 16081 and demonstrates the narrower range of values for the age of the syenites of the Upper Amga district.

The $^{40}Ar/^{39}Ar$ age spectrum of the phlogopite mineral from the lamprophyre sill sample No. 9106 (Fig. 1b) gives the age plateau of 134.9 ± 1.6 Ma (Fig. 3b, Table 3). The plateau contains approximately 92% of cumulative ^{39}Ar, and the age shows that the lamprophyre sills intruded before the formation of syenite bodies in the Upper Amga region.

The $^{40}Ar/^{39}Ar$ spectrum for the K-feldspar of the lamprophyre dike sample No. 17086 (Fig. 1b) indicates that approximately 90% of cumulative ^{39}Ar forms the age plateau for the rocks of 132.3 ± 1.5 Ma (Fig. 3c, Table 4). The present age of the lamprophyre dike together with the previous geochronological data for dike sample No. 13070 (Fig. 1b) shows that the formation of the alkaline dike complex wasclose to the time of the crystallization of syenites in the Upper Amga district, at approximately 132 Ma, and the lamprophyre dikes were also formed at the later stage of the magmatic activity in the range of 117.7 ± 3.4 Ma (Ar-Ar sample No. 13070 data, Ponomarchuk et al., 2019a).

5. Petrography and mineralogy of the alkaline rocks

According to the previous data, the alkaline syenites of the Upper Amga district belong to the high-potassium rocks (Anisimova et al., 2016). In this section, we focused on the detailed petrographic and mineralogical investigations of the main magmatic phases of the syenites and lamprophyres, which associate with the gold mineralization.

The syenites consist of K-feldspar with albite mesoperthites in the matrix and contain phenocrysts of albite, K-feldspar, amphibole, clinopyroxene and phlogopite (Fig. 4a-d). The size of phenocrysts ranges from 1-3 mm to one centimetre. Minor and accessory minerals are apatite, titanite, calcite, magnetite, monazite, epidote, zircon, chlorite and sulfides.

The potassium feldspar is represented by orthoclase (Or_{87-92}), with a small BaO content (up to 1.4 wt.%). The phlogopite flakes have a zonal structure and contain a variable amount of magnesium and iron content (MgO ranges from 13 to 17.3 wt.%, and FeO_t – from 12.7 to 17.4 wt.%), and the chromium content is below the detection limit (Table 5). The magnesium content decreases from the centre to the edge of the phlogopite crystals, while the iron content increases. The amphibole grains (ferro-pargasite and actinolite) also have a zonal structure (Table 6). The composition of clinopyroxene in syenites is

dominated by diopside and enstatite components (Table 6). The mineral is more hedenbergite- and ferrosilite-rich compared to the compositions of clinopyroxene from lamprophyres. The amphibole and clinopyroxene are often replaced by the chlorite (Fig. 4b, d).

Apatite contains up to 1.5 wt.% of F, and as such it can be classified as fluoroapatite; it also contains a mix of chlorine (up to 0.4 wt.%), silica (up to 0.9 wt.% SiO_2) and SO_3 (up to 0.7 wt.%). The mineral is characterized by high amounts of strontium (up to 2.2 wt.% of SrO). Monazite, together with epidote, forms rare inclusions in the feldspar aggregate (Fig. 4c). Monazite is of the cerium variety. Epidote has high concentrations of the light lanthanides (up to 25 wt.% of $LREE_2O_3$).

Lamprophyre sills are porphyritic, less often almost uniformly grained, phlogopite-feldspar rocks with phenocrysts of phlogopite flakes and feldspar crystals (Fig. 4e, f). Occasionally, in thin sections, a dark-coloured mineral, probably amphibole, has been completely replaced by talc aggregate. Minor and accessory minerals, apatite, magnetite, quartz, calcite, albite, oligoclase, sericite, chlorite, titanite, zircon, baddeleyite and sulfide micro-grains and veinlets.

The feldspar is predominantly orthoclase (Or_{82-92}); whereas grains of albite and oligoclase are very rare. As observed in the syenites, the orthoclase, has a high content of BaO (up to 1.7 wt.%). Phlogopite occurs as phenocrysts and micrograins in the matrix; together with orthoclase it is the main rock-forming mineral. The size of the phenocrysts varies from 1-5 mm to several centimetres. The phlogopite has a zonal structure, similar to that of the syenites and the lamprophyre dikes, where the amount of magnesium decreases (from 18.7 to 13.4 wt.% of MgO) from the centre to the grain edge, whereas the iron content increases from 14.2 to 18.1 wt.% of FeO_t (Table 5). The phlogopite is characterized by the high content of BaO (up to 1.4 wt.%), and the chromium content is below the detection limit (Table 5).

Apatite in the lamprophyre sills is also a fluorapatite (up to 1.2 wt.% of F), containing up to 1 wt.% SO_3 and high Sr concentrations of up to 2.1 wt.% SrO. The mineral composition is similar to that of the alkaline syenites and dikes of the lamprophyres. Monazite compositionally corresponds to the cerium variety. Baddeleyite overprints zircon; the size of the mineral grains is up to a few μm. Epidote is characterized by the high content of $LREE_2O_3$ (up to 13 wt.%). The grains of quartz occupy the interstices between the K-feldspar grains. The ore impregnation is represented by the individual grains of sulfides (pyrite, chalcopyrite, etc.); the ore minerals also form cross-cutting micro-veinlets (Fig. 4e, f), as also observed in the lamprophyre dikes.

The lamprophyre dikes are fine-grained rocks, with phenocrysts of olivine and clinopyroxene (Fig. 4g, h). Olivine and clinopyroxene are replaced by chlorite and serpentine. The rim of the magnetite micrograins is noted on the edge of the olivine grains. Porphyritic crystals of olivine and clinopyroxene in the lamprophyre dikes are the main difference between the dikes and the lamprophyre sills. Clinopyroxene composition corresponds to diopside-hedenbergite (Table 6). The mineral has Na_2O impurity (up to 0.5 wt.%, aegirine mineral), titanium (up to 0.8 wt.% TiO_2) and chromium (up to 0.75 wt.% Cr_2O_3). Typically, clinopyroxene and olivine contain small inclusions of apatite crystals. Apatite (with up to 1.5 wt.% of F) is classified as fluorapatite, containing chlorine (up to 0.5 wt.%) and SO_3 (up

to 0.6 wt.%). The mineral is characterized by high amounts of silica (0.7-6 wt.% SiO_2) and strontium (1.7-2.5 wt.% SrO).

The bulk of the rock is composed of feldspars (potassium feldspar Or_{82-87} and albite-oligoclase), and irregularly distributed phlogopite flakes. Magnetite, titanite, elongated-prismatic crystals of the apatite and calcite are evenly distributed. The aggregate of phlogopite scales forms rims around calcite grains (Fig. 4i). Sulfides and calcium amphiboles (pargasite and actinolite) are accessory and minor minerals. Some amphibole grains according to the mineralogical studies are referred to as magnesio-hastingsite and magnesio-ferro-hornblende varieties (Table 6).

The high content of BaO (up to 1.5 wt.%) was determined in the potassium feldspar. The phlogopite, as usual, has a zonal structure, and the central part of the grain; it is characterized by high contents of MgO (up to 16.5 wt.%) and the presence of the chromium (up to 0.3 wt.% Cr_2O_3) (Table 5). At the edge of the grains, decreases in MgO (up to 13 wt.%) and increases in FeO_t (from 13.5 to 19 wt.% outward the centre) content are noted; the chromium is below the detection limit. A special feature of the phlogopite composition of both the central and marginal parts of the grains is the higher TiO_2 (up to 2.7 wt.%) and BaO (up to 1.6 wt.%).

Figure 5 shows that the compositions of mica from the lamprophyre bodies (sills and dikes) overlap those of the mineral from the alkaline syenites. All phlogopites show the evolutionary trends of (1) increasing Fe with slightly increasing or constant Al, and (2) the Ti content increases slightly with respect to that of Al. Both trends generally follow the "minette and alnöite trends" (trends A and M of Mitchell, 1995) for the lamprophyres of the Upper Amga alkaline rocks. According to the classification and nomenclature of lamprophyres based on their mineralogy, where the orthoclase prevails over the plagioclase and the phlogopite and is much larger in rock volume than the hornblende; the lamprophyre bodies of the Upper Amga district can be classified as minettes (Mitchell, 1995).

6. Gold mineralization

According to the geological, geophysical and geochemical works by the geologists of Yakutskgeologiya during 2012-13, linear and area-specific geochemical gold anomalies associated with the late Mesozoic syenite were identified (Sokolov, 2015). The anomalies revealed zones of ore-bearing altered rocks with sulfide mineralization and economically viable gold contents. The gold mineralization is confined to the syenite intrusions and to the contact of the lamprophyres with jasperoids in the Neoproterozoic dolomites (NW of Upper Amga district, Fig. 1b).

The ore-bearing alteration is represented by the quartz-calcite-chlorite rocks with feldspar, apatite and phlogopite grains. The rocks contain gold-sulfide veins (Fig. 6). Sulfide ore minerals include pyrite, chalcopyrite, galena, sphalerite, pyrrhotite, chalcocite, molybdenite and boulangerite. The altered rocks contain also REE-mineral phases – monazite-(Ce) and epidote (see "Petrography and mineralogy of alkaline rocks" section), rutile and thorianite. The gold mineralization includes tellurides of Pb, Ag and Au, and native gold.

Pyrite is characterized by idiomorphic grains, rectangular in cross-section, less often irregular in shape, with scattered disseminations and microveins in the quartz-calcite-chlorite matrix. The size of the grains is up to several centimetres (Fig. 6a-d). EPMA investigations revealed up to 0.5 wt.% Ni in pyrites. The pyrite grains usually contain xenomorphic inclusions of other sulfides, such as chalcopyrite, galena, pyrrhotite, sphalerite, etc. (Fig. 6b-d). Rare sulfides are disseminatied in the quartz-chlorite matrix; the size of inclusions reaches dozens nanometres. Sphalerite in the altered matrix forms solid solution with chalcopyrite (Fig. 6e) (commonly referred to as chalcopyrite decease; Barton and Bethke, 1987).

Chalcopyrite forms interspersed grains of irregular shape and xenomorphic aggregates (up to 10 mm) in the quartz-chlorite matrix, cementing the pyrite grains and microveins in the pyrite crystals. The chalcopyrite is replaced by chalcocite and covellite along grain edges. The irregularly shaped disseminated grains (up to the tens nanometres) of sphalerite, galena, pyrrhotite and boulangerite are in the matrix of alteration. Molybdenite occurs as rare lamellar grains-phenocrysts in the host rock.

Ti-REE mineralization includes minerals, such as rutile, monazite and epidote (see "Petrography and mineralogy of alkaline rocks" section). According to the microprobe analysis, monazite belongs to the cerium variety and contains up to 1 wt.% Th; rutile contains up to 0.9 wt.% V. The boulangerite contains up to 0.9 wt.% As and forms isolated inclusions in the quartz-calcite-chlorite matrix, such as the thorianite grains in the matrix and pyrite crystals (Fig. 6f).

Telluride mineralization is represented by altaite, hessite and petzite (Fig. 6g). The up to 10 μm tellurides crystallize in the form of inclusions in pyrite and quartz-chlorite alteration, often forming xenomorphic aggregates and microveins in quartz. The altaite contains up to 1.63 wt.% Ag; the hessite in the granular aggregates contains up to 4.9 wt.% Au.

Native gold was recognized in quartz veins hosted in the quartz-calcite-chlorite alteration (Fig. 5h, i); the gold constitutes rounded and drop-shaped grains in the form of microveins in quartz of altered rocks. The size of the grains is usually 15-20 μm, while the veins are tens μm wide. According to the microprobe analysis, the native gold reveals high fineness, with 0.39-2.34 wt.% Ag.

7. Fluid inclusions study

Fluid inclusions (FI) were studied in quartz from quartz-calcite-chlorite alteration. The optical microscope investigations revealed the following types of fluid inclusions, according to their phase composition (Fig. 7): 1) gas-liquid FI with a solid phase – VLS-type; 2) gas-liquid FI with a liquid CO_2 phase – VLC-type; and 3) gas-liquid FI – VL-type. We identified and investigated the primary and pseudo-secondary FI (Roedder, 1984), which participated in the ore formation.

The primary FI are rounded and isometric in shape of the negative vacuole crystals (Fig. 7a, b); they are recorded as isolated inclusions randomly distributed within the matrix grains. The size of the primary FI varies within a narrow range of 10-15 μm. Pseudo-secondary inclusions of the irregular or isometric shape, in the healed cracks within the individual quartz grains, are 7-20 μm in size (Fig. 7c). The primary

VLS and VLC and pseudo-secondary VL FI occur in the quartz grains that host sulfide and gold mineralization.

The gas phase of the primary VLS FI contains CO_2 with up to 1.5 vol.% N_2. Mineral phases are represented by the isotropic light-coloured cubic crystals of the Na- or K-chlorides (Fig. 7a). Inclusions are identified in the individual idiomorphic quartz grains and interstitial aggregates and veins (Qz-1) located between feldspar, calcite and chlorite minerals, containing scattered sulfides (Fig. 6a, b). The homogenization temperatures (T_h) of the VLS FI are 370-390°C; and salinity estimates are 42-44 wt.% NaCl-eq. (Table 7). The pseudo-secondary VL-type FI in the quartz (Qz-1) in the gas phase also contains CO_2 and N_2 (up to 4 vol.%); and sometimes the FIs contain microscopic particles of ore phases. For the pseudo-secondary FI, the homogenization temperatures are in the range of 330-350°C. The ice melting temperature (T_m) is -20...-10 °C, which corresponds to a salinity of 14-22.7 wt.% NaCl-eq. (Table 7).

The primary gas-liquid VLC FIs (Fig. 7b) were identified in quartz aggregates and microveins (Qz-2), cross-cutting grains of feldspar, chlorite minerals, carbonate and quartz (Qz-1). For the VLC FI in the ore-quartz (Qz-2), the homogenisation temperatures of CO_2 and inclusions are 28-30 °C and 340-360°C, respectively (Table 7). According to these data, the density of CO_2 was calculated as 0.34 g/cm^3 and the pressure in the fluid was measured as about 1150 bar (using the FLINCOR software). For the pseudo-secondary VL-type FI in quartz (Qz-2) with telluride and gold mineralization (Fig. 6h, i; Fig. 7c), the composition of the gas phase was detected as $CO_2 \pm N_2$. The homogenization temperature of the FI varies from 210 to 230°C; and the T_m interval is -6...-2°C, which corresponds to the salinity of 3.3-9.2 wt.% NaCl-eq. (Table 7).

8. Discussion

8.1. Sequence of rocks and ore-mineralization formation in the Upper Amga gold district

The simplified geological setting of the late Mesozoic alkaline rocks and formation conditions of the associated sulfides and gold mineralization are shown in Fig. 8.

According to the geological and geochronological data, the syenite bodies were emplaced between the lamprophyre sills and dikes. The ages of the syenite intrusions are 131.4 ± 2.9 Ma (sample No. 16081) and 131.4 ± 1.5 Ma (sample No. 5088) according to the U-Pb and Ar-Ar data, respectively. The lamprophyre sills were formed before syenites at 134.9 ± 1.6 Ma (sample No. 9106, Ar-Ar present data). In addition, the lamprophyre dike complex crystallized within the age range of the syenite intrusions at 132.3 ± 1.5 Ma (sample No. 17086, the Ar-Ar present data); and the next episode was after syenites at 117.7 ± 3.4 Ma (sample No. 13070, Ar-Ar data Ponomarchuk et al., 2019a). The dikes and stocks of the ultramafic and alkaline mafic rocks were formed during the earlier stage, whilst the aegirine granites were crystallized during the last stage of the late Mesozoic activity (Fig. 8).

Three types of mineralization were established in the main phases of the Upper Amga alkaline magmatic rocks. The first Ti-REE-Th mineralization is represented by the accessory and secondary

magmatic minerals of the syenites and lamprophyres – REE-epidote, monazite-(Ce), titanite and rutile; thorianite was formed during the late hydrothermal stage (Fig. 8). The second type is polymetallic Fe-Cu-Zn-Ni-Pb-Mo-Sb-As-S sulfide mineralization (pyrite, chalcopyrite, galena, sphalerite, pyrrhotite, chalcocite, molybdenite and boulangerite). The sulfide minerals were generated by hydrothermal fluids characterized by a NaCl-H_2O composition and 44-22.7 wt.% NaCl-eq. The gas phase of the fluids contains CO_2 with some N_2; the sulfide minerals formed in two stages at 390-370°C and 360-340°C (Fig. 8). The sulfide mineralization is hosted in quartz veins and in the matrix of the altered rocks within the syenite intrusions and lamprophyre bodies.

The third type of gold epithermal mineralization is characterized by the tellurides of Au, Ag and Pb, as well as native gold grains and microveins in altered rocks. Altaite, hessite, petzite and native gold occur in the later quartz grains and microveins, cross-cutting the quartz-sulfide assemblages and quartz-chlorite alteration. The mineralization precipitated from the low-concentration and low-temperature CO_2±N_2-NaCl-H_2O fluids at 230-210°C homogenization temperature with a salinity of 9.2-3.3 wt.% NaCl-eq. (Fig. 8). The decrease in temperatures of mineralization and the concentration of the solutions during the evolution of the hydrothermal system indicates mixing and diluting of the fluids with meteoric waters. In addition, the system has a group of essentially gaseous inclusions with carbonic acid in the composition, which gives estimates for the pressure of the ore-bearing fluids at 1150 bar suggesting that boiling processes might have occurred.

The proposed model for the formation of the late Mesozoic gold mineralization in the Upper Amga district of the Aldan-Stanovoy shield can be compared to the model for the Cretaceous gold deposits in the Jiaodong Peninsula in the eastern part of the North China craton (Yang and Santosh, 2015). According to Khomich et al. (2014), the margins of the Siberian and North China cratons are confined to the periphery of the same stagnant oceanic slab and the mantle upwelling (as mentioned in the Introduction). The geochronological data of the Mesozoic alkaline magmatism in the Aldan-Stanovoy shield correlate with the Mesozoic magmatic activity in the North China craton (Wang, 2012; Yang and Santosh, 2015). The dehydration and decarbonatization of the subducting slab and overlying sediments, considered as the ultimate source of the ore-forming components, was also proposed by Goldfarb and Santosh (2013). Further study of petrology and geochronology of the Mesozoic gold-bearing alkaline magmatism of Siberian craton and correlation with the Mesozoic complexes of the North China craton is required to specify the structure, geodynamics and metallogeny of the activated margins of the cratons and adjacent orogens.

8.2. Geochronology of Mesozoic gold mineralization in the Aldan-Stanovoy shield

Within the Chara-Aldan metallogenic province (see Introduction), geochronology of late Mesozoic magmatism, petrology of the rocks and associated Au-U-Mo-PGE mineralization are best studied in the Central Aldan district (Fig. 9). According to Maximov et al. (2010), the Mesozoic alkaline magmatism in the Central Aldan district occurred in four stages, forming a continuous series with systematic

variations. The K-Ar data constrain the following stages: (1) Early Jurassic monzonite – syenite at 217-186 Ma; (2) Middle Jurassic dunite and leucitite – alkaline syenite at 176-161 Ma; (3) Late Jurassic-Early Cretaceous fergusite – dunite and monzonite – syenite at 162-140 Ma; and (4) Early Cretaceous monzonite – syenite and leucite – alkaline syenite at 138-125 Ma. This classification is largely based on inaccurate K-Ar dating.

Recent Ar-Ar and U-Pb data showed that the gold deposits of the Central Aldan district (e.g., Ryabinovoe, Lebedinoe and Kuranakh) were formed during several stages between 160 and 120 Ma (Borisenko et al., 2011). According to Ar-Ar dating, most of the alkaline rocks (sills, stocks, ring-type intrusions and volcanic rocks) formed between 160 and 135 Ma, whereas the formation of the dike complex of lamprophyric minettes and syenite porphyries, intrusions of alkaline picrites, shonkinites, and related took place at 135-120 Ma. The main productive stages of the Ryabinovoe, Kuranakh and Lebedinoe deposits fall within the narrow range at approximately 137 Ma, which suggests their simultaneous formation in different parts of the Central Aldan alkaline complex (Borisenko et al., 2011).

Shatov et al. (2012) showed almost identical crystallization age (147-120) of the syenites and lamprophyres of the Ryabinovoe deposit. According to U-Pb and Ar-Ar dating, the age of ultramafic and alkaline rocks of the Inagli Complex in the Central Aldan district falls into the interval of 144–128 Ma (Borisenko et al., 2011; Ponomarchuk et al., 2019b). The U-Pb dating of the Elkon gold-uranium ore-magmatic system within Central Aldan showed that the magmatic and hydrothermal activity took place at 143-125 Ma (Kazansky, 2004; Terekhov, 2012). According to Ar-Ar dating of phlogopite from syenites of the Lunnoe deposit (in the southwestern part of the Elkon mineral cluster), the rocks were formed at 143.1 ± 2.0 Ma. Thus, the evolution of the Mesozoic alkaline ore-magmatic systems in the Central Aldan district took place at 160-120 Ma, with main productive phase of 145-120 Ma (Fig. 9).

The Tyrkanda gold district is located in the southeastern part of the Chara-Aldan metallogenic province (Fig. 9). According to Rb-Sr and Ar-Ar dating, the age of the rocks from the Dzheltula alkaline massif falls within the interval of 138-115 Ma (Kravchenko et al., 2014), and the main alkaline phases of the massif and the dike complex fit within the rather narrow interval of 122-118 Ma (Ar-Ar data, Prokopyev et al., 2018).

The U-Pb isotopic data on zircon and titanite from the subalkaline magmatic rocks in the Ketkap-Yuna ore-magmatic system (Ket-Kap mineral district, Fig. 9) suggest that the Mesozoic magmatism continued only during few million years in the Early Cretaceous (Polin et al., 2012). In particular, the age of the Uchur Complex is 124-120 Ma, and the age of the Ket-Kap monzonites is 126-124 Ma (Fig. 9).

The age of the syenites and lamprophyre bodies within the investigated Upper Amga gold district is approximately 135-117 Ma. This correlates with the data from the Chara-Aldan metallogenic province and is similar to the rocks of the Tyrkanda district (Fig. 9). Moreover, the mineral compositions of the rocks and the geological settings of the Upper Amga and Tyrkanda districts are also similar.

The alkaline rocks of the Tyrkanda district are located within the Tyrkanda tectonic mélange zone (Fig. 1a) (Kravchenko et al., 2014; Prokopyev et al., 2018). The Dzheltula alkaline complex in the

Tyrkanda district is composed of several rock phases of syenite composition, and a large number of porphyritic syenite dikes, quartz syenites and lamprophyres (minettes) are concentrated within the complex. In addition, the similarity for the Upper Amga and Tyrkanda alkaline complexes can be seen in the mineral composition and formation conditions of the gold-bearing alteration. The alteration is localized in the contact areas of the intrusive bodies and within the fault zones, which are controlled by the ancient regional faults (Fig. 1a, b). These fault zones are traced by the numerous dikes of the alkaline rocks, such as syenites and lamprophyres.

8.3. Evidence of magmatic activity in the Aldan shield between 2.5-2.2 and 1.9-1.87 Ga

The U-Pb SIMS zircon dating of the syenites (No. 16081) from the Upper Amga district identified three clusters that correspond to the intervals of approximately 2.5-2.2, 1.9-1.87 and 0.13 Ga (Fig. 2b). The age of the syenite crystallization is 131.4 ± 2.9 Ma (Fig. 2c), coinciding with the obtained Ar-Ar data. Below, we consider the geological events within the Aldan shield that occurred at 2.5-2.2 and 1.9-1.87 Ga, and which can be recorded in the age characteristics of the investigated zircons.

The central portion of the Aldan shield hosts Archean and Paleoproterozoic granitoids (Kotov, 2003; Kotov et al., 1995, 2004a,b, 2005; Parfenov and Kuzmin, 2001; Sal'nikova, 1993; Sal'nikova et al., 1997; Velikoslavinskii et al., 2011) (Fig. 1). In the western part of the Nimnyr granulite-orthogneiss terrane, near the Amga mélange zone (Central-Aldan superterrane, Fig. 1a), the biotite and leucocratic subalkaline granites, leucocratic granites and subalkaline leucogranites were emplaced at around 2487 ± 5 Ma (zircon, U-Pb data; Sal'nikova, 1993). The age of the biotite-amphibole gneiss and pegmatoid granites within the Amga mélange zone is 2484 ± 5 Ma (zircon U-Pb and Pb-Pb data; Sal'nikova, 1993). At this time, the anorogenic granites of the Nelyukin Complex (2398-2522 Ma) and picrite dikes (2202 ± 41 Ma) were intruded in the Aldan-Stanovoy shield (Kotov, 2003). At 1.87-1.9 Ga the leucosome from the migmatites of the Amga mélange zone was formed, with the age of 1895 ± 4 Ma (U-Pb on zircon; Nutman et al., 1992), as well as the dike of the aplite granites in the Central Aldan district, with the age of 1907 ± 15 Ma (zircon, U-Pb; Sal'nikova, 1993). From 1966 ± 4 to 1925 ± 5 Ma, the formation of crustal-scale thrusts took place within the viscous Amga mélange zone and related northwestern and submeridional linear folds (Kotov, 2003).

The emplacement of the Seligdar magnesiocarbonatites at the Central Aldan district took place at 1880 ± 13 Ma (U-Pb zircon data; Prokopyev et al., 2017). The intrusion of the carbonatites was coeval with late Paleoproterozoic (1.88-1.85 Ga) post-collisional processes in the Siberian craton (e.g., Gladkochub et al., 2006, 2012). Mafic dike swarms in the Aldan and Irkutsk promontory regions and basalts from the volcanoplutonic belt in the Baikal uplift were formed between 1.86-1.87 and 1.84 Ga, respectively (Ernst et al., 2016; Shokhonova et al., 2010). Recent geochronological studies constrained the ages of layered ultramafic-mafic complexes at 1.86-1.88 Ga in the southern part of Siberia (Mekhonoshin et al., 2016; Popov et al., 2009; Tolstykh et al., 2008). In addition, numerous granitic intrusions and acidic volcanic rocks within the Siberian craton are also of similar age (e.g., Donskaya et

al., 2005; Larin et al., 2000; Neimark et al., 1998; Nozhkin et al., 2003; Turkina et al., 2003). The age of formation of the Seligdar magnesiocarbonatites suggests a link with mafic and felsic rocks of the Kalar-Nimnyr-Malozadoilarge igneous province in Siberia (Ernst and Bell 2010; Ernst et al. 2016).

However, the geochemical study of the Seligdar carbonatites reveals that the magnesiocarbonatites are dominated by a component that was derived from an enriched mantle source which was separated from the depleted mantle at ca. 2.7-2.5 Ga (Doroshkevich et al., 2018). Ariskin et al. (2015) also noted a similar evolution of the mantle source of the Yoko-Dovyren dunite-troctolite-gabbro-norite layered complex (northern Baikal area), and Doroshkevich et al. (2018) concluded that the primary magmas were produced by melting of the 2.8-2.7 Ga mantle source. Doroshkevich et al. (2018) reported that Seligdar carbonatites, Paleoproterozoic Chiney layered gabbro intrusion from the western part of the Aldan shield (Gongalsky et al., 2008), Neoarchean Khani lamproites from the Aldan-Stanovoy shield (Vladykin et al., 2005) and late Mesozoic high-K intrusions (Bogatikov et al., 1994) plot on the same εNd evolutionary trend. In our opinion, repeated melting of the enriched source could have occurred during the late Mesozoic and was accompanied by formation of numerous high-K alkaline rocks, such as those in the Upper Amga Complex in the Aldan shield (Doroshkevich et al., 2018).

9. Conclusions

1. The main late Mesozoic alkaline magmatic phases of the Upper Amga district are represented by syenite and porphyritic syenite- stocks and sills as well as lamprophyre sills and dikes.
2. The age of the syenites is 131.4 ± 1.5 (2.9) Ma. The lamprophyre sills and dykes intruded at 134.9 ± 1.6, – 132.3 ± 1.5 and 117.7 ± 3.4 Ma.
3. The hydrothermally altered alkaline rocks host sulfides and economically viable gold mineralization. Three types of mineralization are present in the hydrothermally altered alkaline rocks: REE-Ti-Th, polymetallic (sulfide) and telluride-gold.
4. Fluid inclusion studies reveal that sulfides were formed from the highly concentrated 44-22.7 wt.% NaCl-eq. hydrothermal fluids of CO_2-N_2–NaCl-H_2O composition at 390-340°C; the epithermal telluride-gold mineralization was formed from low-temperature CO_2±N_2-NaCl-H_2O fluids, with a homogenization temperature of 230-210°C and low salinity of 9.2-3.3 wt.% NaCl-eq.

Acknowledgements

The mineralogical and petrographic investigations and Ar–Ar dating of the syenites were supported by the Russian Foundation for Basic Research project No. 18-45-140002; the U-Pb SIMS analyses of the syenites, ore mineralogy, fluid inclusion study and Ar-Ar geochronology of the lamprophyre intrusions were done on state assignment of the Sobolev Institute of Geology and Mineralogy, Siberian Branch of the Russian Academy of Science (0330-2016-0002) and was also partially financially supported by the

Russian Science Foundation (19-17-00019). The lithosphere evolution investigations were supported by the research projects of the Russian Institute of Diamond and Precious Metal Geology, Siberian Branch of the Russian Academy of Science (No 0381-2019-0001 and 0381-2019-0003). We thank Dr. Alexander Yakubchuk, Prof. Franco Pirajno and reviewers for their comments and recommendations, which led to significant improvement of the manuscript.

References

Anisimova, G.S., Zaitsev, A.I., Sokolov, E.P., 2016. Rb-Sr systematics of the rocks of Upper Amga region (Yakutia), in: Polufuntikova, L.I., Geology and mineral resources of the Northeast Asia (Abstract volume). The Publishing House of the NEFU, Yakutsk, 19-23 (in Russian).

Ariskin, A.A., Danyushevsky, L.V., Konnikov, E.G., Maas, R., Kostitsyn, Yu.A., McNeill, A., Meffre, S., Nikolaev, G.S., Kislov, E.V., 2015. The Dovyren intrusive complex (Northern Baikal Region, Russia): isotope-geochemical markers of contamination of parental magmas and extreme enrichment of the source. Russ. Geol. Geophys. 56 (3), 528-556. https://doi.org/10.1016/j.rgg.2015.02.004.

Barton, P.B., Bethke, P.M., 1987. Chalcopyrite disease in sphalerite: pathology and epidemiology. Am. Mineral. 72, 451-467.

Baksi, A.K., Archibald, D.A., Farrar, E., 1996. Intercalibration of $^{40}Ar/^{39}Ar$ dating standards. Chem. Geol. 129, 307-324. https://doi.org/10.1016/0009-2541(95)00154-9.

Bilibin, Yu. A., 1959. Some interesting features of the Aldan metallogeny, in: Selected works by Yu.A. Bilibina, Volume 2, AN SSSR, Moscow, pp. 344-347 (in Russian).

Black, L.P., Kamo, S.L., Allen, C.M., 2003. TEMORA 1: a new zircon standard for Phanerozoic U-Pb geochronology. Chem. Geol. 200, 155-170. https://doi.org/10.1016/S0009-2541(03)00165-7.

Bodnar, R.J. and Vityk, M.O., 1994. Interpretation of Microthermometric Data for H_2O-NaCl Fluid Inclusions, in: De Vivo, B., Frezzotti, M.L. (Eds.), Fluid Inclusions in Minerals: Methods and Application. Virginia Tech, Blacksburg, pp. 117-130.

Bogatikov, O.A., Kononova, V.A., Pervov, V.A., Zhuravlev, D.Z., 1994. Petrogenesis of Mesozoic Potassic Magmatism of the Central Aldan: a Sr-Nd isotopic and geodynamic model. Int. Geol. Rev. 36 (7), 629-644. https://doi.org/10.1080/00206819409465479

Borisenko, A.S., 1977. Study of the salt composition of solutions of gas-liquid inclusions in minerals by cryometric method. Russ. Geol. Geophys. 18, 16-27 (in Russian).

Borisenko, A.S., Gas'kov, I.V., Dashkevich, E.G., Okrugin, A.M., Ponomarchuk, A.V., Travin, A.V., 2011. Geochronology of magmatic processes and ore-formation in the Central Aldan Gold-Ore Region, in: Gladkochub, D.P., Donskaya, T.V., Large Igneous Provinces of Asia: Mantle Plumes and Metallogeny (Abstract volume), Petrographica, Irkutsk, pp. 38-39.

Donskaya, T.V., Gladkochub, D.P., Kovach, V.P., Mazukabzov, A.M., 2005. Petrogenesis of Early Proterozoic postcollisional granitoids in the southern Siberian craton. Petrol. 13 (3), 253-279.

Doroshkevich, A.G., Prokopyev, I.R., Izokh, A.E., Klemd, R., Ponomarchuk, A.V., Nikolaeva, I.V., Vladykin, N.V., 2018. Isotopic and trace element geochemistry of the Seligdar magnesiocarbonatites (South Yakutia, Russia): Insights regarding the mantle evolution beneath the Aldan-Stanovoy shield. Journal of Asian Earth Sciences 154, 354-368. https://doi.org/10.1016/j.jseaes.2017.12.030

Dvornik, G.P., 2009. Sericite-microcline metasomatites and gold mineralization of the Ryabinovsky ore field (Aldan Shield). Litosfera 2, 56-66 (in Russian).

Dzevanovskii, Yu.K., Vorona, I.D., Lagzdina, G.Yu., 1972. Geological Map of the Southern Yakutsk ASSR. Kartfabrika VATT, Leningrad (in Russian).

Ernst, R.E., Bell, K., 2010. Large igneous provinces (LIPs) and carbonatites. Mineral. Petrol. 98, 55-76. https://doi.org/10.1007/s00710-009-0074-1.

Ernst, R.E., Hamilton, M.A., Söderlund, U., Hanes, J.A., Gladkochub, D.P., Okrugin, A.V., Kolotilina, T., Mekhonoshin, A.S., Bleeker, W., Le Cheminant, A.N., Buchan, K.L., Chamberlain, K.R., Didenko, A.N., 2016. Long-lived connection between southern Siberia and northern Laurentia in the Proterozoic. Nat. Geosci. 9, 464-469. https://doi.org/10.1038/ngeo2700.

Gladkochub, D.P., Donskaya, T.V., Ernst, R., Mazukabzov, A.M., Sklyarov, E.V., Pisarevsky, S.A., Wingate, M., Söderlund, U., 2012. Proterozoic basic magmatism of the Siberian craton: main stages and their geodynamic interpretation. Geotectonics 46 (4), 273-284. https://doi.org/10.1134/S0016852112040024.

Gladkochub, D.P., Pisarevsky, S.A., Donskaya, T.V., Natapov, L.M., Mazukabzov, A.M., Stanevich, A.M., Sklyarov, E.V., 2006. The Siberian craton and its evolution in terms of the Rodinia hypothesis. Episodes 29 (3), 169-174.

Goldfarb, R.J., Taylor, R.D., Collins, G.S., Goryachev, N.A., Orlandini, O.F., 2014. Phanerozoic continental growth and gold metallogeny of Asia. Gondwana Res. 25, 48-102. https://doi.org/10.1016/j.gr.2013.03.002.

Goldfarb, R., Santosh, M., 2013. The dilemma of the Jiaodong gold deposits: are they unique? Geosci. Front. 5 (2), 139-153. https://doi.org/10.1016/j.gsf.2013.11.001.

Gongalsky, B.I., Sukhanov, M.K., Goltzman, Yu.V., 2008. Sm-Nd system of Chiney anorthozite-gabbro-norithe pluton (East Transbaikalia), in: Problems of Ore Geology Deposits, Mineralogy, Petrology and Geochemistry. IGEM RAS, Moscow, pp. 57-60. https://www.scopus.com/record/display.uri?eid=2-s2.0-84924677336&origin=inward

Goryachev, N.A., Pirajno, F, 2014. Gold deposits and gold metallogeny of Far East Russia. Ore Geology Reviews 59, 123-151. https://doi.org/10.1016/j.oregeorev.2013.11.010.

Guo, P., Santosh, M., Li, S.R., 2013. Geodynamics of gold metallogeny in the Shandong Province, NE China: an integrated geological, geophysical and geochemical perspective. Gondwana Res. 24, 1172-1202. https://doi.org/10.1016/j.gr.2013.02.004.

Kazansky, V.I., 2004. The unique Central Aldan gold-uranium ore district (Russia). Geol. Ore Deposits 46 (3), 167-181.

Khatylaev, M.M., 1972. Gold Mining Industry of Yakutia (1923-1937 years). Yakutsk Publishing House, Yakutsk (in Russian).

Khomich, V.G., Boriskina, N.G., Santosh, M., 2014. A geodynamic perspective of world-class gold deposits in East Asia. Gondwana Res. 26 (3-4), 816-833. https://doi.org/10.1016/j.gr.2014.05.007.

Khomich, V.G., Boriskina, N.G., Santosh, M., 2015. Geodynamics of Late Mesozoic PGE, Au, and U mineralization in the Aldan Shield, North Asian Craton. Ore Geology Reviews 68, 30-42. https://doi.org/10.1016/j.oregeorev.2015.01.007.

Kochetkov, A.Ya., 2006. Mesozoic gold-bearing ore-magmatic systems of Central Aldan. Russ. Geol. Geophys. 47 (7), 835-846.

Kotov, A.B., 2003. Boundary conditions of geodynamic models of the continental growth of the Aldan Shield, PhD thesis, SPbGU, St. Petersburg, 79 (in Russian).

Kotov, A.B., Anisimova, I.V., Glebovitsky, V.A., Kovach, V.P., Sal'nikova, E.B., Smelov, A.P., Berezkin, V.I., Zagornaya, N.Yu., 2004a. Age limits of the greenstone belts of the Western Aldan shield. Doklady Earth Sciences 399 (8), 1060-1064.

Kotov, A.B., Kovach, V.P., Sal'nikova, E.B., 1995. Continental crust age and formation stages in the central. Aldan granulite-gneiss terrain: U-Pb and Sm-Nd isotopic data for granitoids. Petrol. 3, 87-97.

Kotov, A.B., Glebovitsky, V.A., Kazansky, V.I., Sal'nikova, E.B., Pertsev, N.N., Kovach, V.P., Yakovleva, S.Z., 2005. Age boundaries of the formation of major structures in the Central Aldan shield. Doklady Earth Sciences 405 (8), 1155-1158.

Kotov, A.B., Sal'nikova, E.B., Larin, A.M., Kovach, V.P., Savatenkov, V.M., Yakovleva, S.Z., Berezhnaya, N.G., Plotkina, Yu.V., 2004b. Early Proterozoic granitoids in the Junction zone of the Olekma granite-greenstone belt and the Aldan granulite-gneiss terrane, Aldan shield: age, sources, and geodynamic environments. Petrol. 12 (1), 37-55.

Kravchenko, A.A., Ivanov, A.I., Prokopyev, I.R., Zaitsev, A.I., Bikbaeva, E.E., 2014. Composition and age of the Mesozoic intrusions of the Tyrkanda ore district of the Aldan-Stanovoy shield, Otechestvennaya Geol. 5, 43-52 (in Russian).

Lavrent'ev, Y.G., Karmanov, N.S., Usova, L.V., 2015. Electron probe microanalysis of minerals: Microanalyzer or scanning electron microscope? Russ. Geol. Geophys. 56 (8), 1154-1161. https://doi.org/10.1016/j.rgg.2015.07.006.

Larin, A.M., Kotov, A.B., Sal'nikova, E.B., Kovach, V.P., Makarev, L.B., Timashkov, A.N., Berezhnaya, N.G., Yakovleva, S.Z., 2000. New data on the age of granites of the Kodar and Tukuringra complexes, eastern Siberia: geodynamic constraints. Petrol. 8 (3), 267-279.

Ludwig, K.R., 1999. User's manual for Isoplot/Ex, version 2.10, a geochronological toolkit for microsoft excel. Berkeley Geochronology Center Special Publication, Berkeley.

Ludwig, K.R., 2000. SQUID 1.00, A User's Manual. Berkeley Geochronology Center Special Publications, Berkeley.

Maximov, E.P., 2003 Mesozoic ore-bearing igneous systems of the Aldan-Stanovoy shield. PhD thesis, Technical Institute (branch) of the Yakutsk State University in Neryungri, Yakutsk, 385 (in Russian).

Maximov, E.P., Uyutov, V.I., Nikitin, V.M., 2010. The Central Aldan Gold-uranium ore magmatogenic system, Aldan-Stanovoy Shield, Russia. Russ. J. Pac. Geol. 4 (2), 95-115. https://doi.org/10.1134/S1819714010020016.

Mekhonoshin, A.S., Ernst, R., Soderlund, U., Hamilton, M.A., Kolotilin, A.T.B., Izokh, A.E., Polyakov, G.V., Tolstykh, N.D., 2016. Relationship between platinum-bearing ultramafic-mafic intrusions and large igneous provinces (exemplified by the Siberian craton). Russ. Geol. Geophys. 57 (5), 822-833. https://doi.org/10.1016/j.rgg.2015.09.020.

Mitchell, R.H., 1995. Kimberlites, Orangeites and Related Rocks. Plenum Press, New York.

Neimark, L.A., Larin, A.M., Nemchin, A.A., Ovchinnikova, G.V., Rytsk, E.Y., 1998. Geochemical, geochronological (U-Pb) and isotopic (Pb, Nd) evidence of anorogenic magmatism in the North Baikal volcanoplutonic belt. Petrol. 6 (4), 139-164.

Nozhkin, A.D., Bibikova, E.V., Turkina, O.M., Ponomarchuk, V.A., 2003. U-Pb, Ar-Ar, and Sm-Nd isotope-geochronological study of porphyritic subalkalic granites of the Taraka pluton (Yenisei Range). Russ. Geol. Geophys. 44 (9), 879-889.

Nutman, A.P., Chernyshev, I.V., Baadsgaard, H., Smelov, A.P., 1992. The Aldan Shield of Siberia USSR: the age of its Archean components and evidence for widespread reworking in the mid-Proterozoic. Precambrian Res. 54 (4), 195-209. https://doi.org/10.1016/0301-9268(92)90070-5.

Parfenov, L.M., Kuzmin, M.I., 2001. Tectonics, Geodynamics and Metallogeny of the Territory of the Republic of Sakha (Yakutia). Nauka/Interperiodika, Moscow (in Russian).

Pirajno, F., Santosh, M., 2014. Rifting, intraplate magmatism, mineral systems and mantle dynamics in central-east Eurasia: an overview. Ore Geology Reviews 63, 265-295. https://doi.org/10.1016/j.oregeorev.2014.05.014.

Polin, V.F., Mitsuk, V.V., Khanchuk, A.I., Glebovitskii, V.A., Budnitskii, S.Yu., Rizvanova, N.G., Solyanik, A.N., Shishov, A.S., 2012. Geochronological limits of subalkaline magmatism in the Ket-Kap – Yuna igneous province, Aldan Shield. Doklady Earth Sciences 442 (1), 17-23. https://doi.org/10.1134/S1028334X12010096.

Ponomarchuk, A.V., Prokopyev, I.R., Doroshkevich, A.G., Yegitova, I.V., Kravchenko, A.A., Ivanov A.I., 2019a. $^{40}Ar/^{39}Ar$ age of alkaline rocks of the Upper Amga massif (Aldan shield, South Yakutia). Bulletin of Tomsk Polytechnic University, Geo Assets Engineering 2 *in press*.

Ponomarchuk, A.V., Prokopyev, I.R., Svetlitskaya, T.V., Doroshkevich, A.G., 2019b. $^{40}Ar/^{39}Ar$ geochronology of alkaline rock of the Inagly massif (Aldan shield, South Yakutia**).** Russ. Geol. Geophys. *in press*.

Popov, N.V., Kotov, A.B., Postnikov, A.A., Sal'nikova, E.B., Shaporina, M.N., Larin, A.M., Yakovleva, S.Z., Plotkina, Y.V., Fedoseenko, A.M., 2009. Age and tectonic position of the Chiney Layered Massif, Aldan shield. Doklady Earth Sciences 424 (1), 64-67. https://doi.org/10.1134/S1028334X09010139.

Prokopyev, I.R., Doroshkevich, A.G., Ponomarchuk, A.V., Sergeev, S.A., 2017. Mineralogy, age and genesis of apatite-dolomite ores at the Seligdar apatite deposit (Central Aldan, Russia). Ore Geol. Rev. 81, 296-308. https://doi.org/10.1016/j.oregeorev.2016.10.012.

Prokopyev, I.R., Kravchenko, A.A., Ivanov, A.I., Borisenko, A.S., Ponomarchuk, A.V., Zaitsev, A.I., Kardash, E.A., Rozhkov, A.A., 2018. Geochronology and ore mineralization of the Dzheltula alkaline massif (Aldan Shield, South Yakutia). Russ. J. Pac. Geol. 12 (1) 34-45. https://doi.org/10.1134/S1819714018010062.

Roedder, E., 1984. Fluid inclusions. In: Ribbe, P.H. (ed.), Reviews in Mineralogy (vol. 12). Mineralogical Society of America, 644.

Sal'nikova, E.B., 1993. Tectono-magmatic evolution of the northern flank of the junction zone of the Olekma granite-greenstone and Aldan granulite-gneissic regions of the Aldan Shield, PhD thesis, Institute of Geology and Geophysics, Russian Academy of Sciences, St.-Petersburg, 16 p. (in Russian).

Sal'nikova, E.B., Kotov, A.B., Belyatsky, B.V., 1997. U-Pb ages of granitoids at the lunction of the Olekma granite-greenstone and Aldan granulite-gneis zones. Stratigraphy and geological correlation 5 (2), 101-109.

Shatov, V.V., Molchanov, A.V., Shatova, N.V., Sergeev, S.A., Belova, V.N., Terekhov, A.V., Radkov, A.V., Soloviev, O.L., 2012. Petrography, geochemistry and isotope dating (U-Pb and Rb-Sr) of alkaline igneous rocks of the Ryabinovy Massif (Southern Yakutia). Regional Geology and Metallogeny 51, 62-78 (in Russian).

Shokhonova, M.N., Donskaya, T.V., Gladkochub, D.P., Mazukabzov, A.M., Paderin, I.P., 2010. Paleoproterozoic basaltoids in the North Baikal volcanoplutonic belt of the Siberian craton: age and petrogenesis. Russ. Geol. Geophys. 51 (8), 815-832. https://doi.org/10.1016/j.rgg.2010.07.001.

Sokolov, E.P., 2015. Ore gold of the Upper Amga gold-bearing regon, in: Biller, A.Ya (Ed.), Geology and mineral resources of the Northeast of Russia (Abstract volume). The Publishing House of NEFU, Yakutsk, pp. 458-462 (in Russian).

Terekhov, A.V., 2012. Ore potential of hydrothermal-metasomatic formations of the Elkon gold-uranium ore cluster, PhD thesis, AP Karpinsky Russian Geological Research Institute, St.-Petersburg, 220 (in Russian).

Tolstykh, N.D., Orsoev, D.A., Krivenko, A.P., Izoch, A.E., 2008. Noble Metals in Layered Ultrabasic-Basic Massifs in the Southern Part of Siberian Platform. Parallel, Novosibirsk (in Russian).

Travin, A.V., Yudin, D.S., Vladimirov, A.G., Khromykh, S.V., Volkova, N.I., Mekhonoshin, A.S., Kolotilina, T.B., 2009. Thermochronology of the Chernorud granulite zone, Ol'khon region, Western Baikal. Geochem. Int. 47 (11), 1181-1199. https://doi.org/10.1134/S0016702909110068.

Turkina, O.M., Bibikova, E.V., Nozhkin, A.D., 2003. Stages and geodynamic settings of Early Proterozoic granite formation on the southwestern margin of the Siberian craton. Doklady Earth Sciences 389 (2), 159-163.

Velikoslavinskii, S.D., Kotov A.B., Tolmacheva, E.V., Sal'nikova, E.B., Kovach, V.P., Larin, A.M., 2011. Early Precambrian granite-gneiss complexes in the Central Aldan Shield. Petrol. 19 (4), 382-398. https://doi.org/10.1134/S0869591111040060.

Vetluzhskikh, V.G., 1990. Gold mineralization of the epoch of Mesozoic tectonic-magmatic activation of the Aldan-Stanovoy province, PhD thesis, Moscow-Yakutsk, 325 (in Russian).

Vetluzhskikh, V.G., Kazanskii, V.I., Kochetkov, A.Ya, Yanovskii, V.M., 2002. Central Aldan gold deposits. Geol. Ore Deposits 44 (6), 405-434.

Vladykin, N.V., Morikyo, T., Miuazaki, T., 2005. Geochemistry of Sr and Nd isotopes in the carbonatites of Siberia and Mongolia and some geodynamic implications, in: Vladykin, N.V. (Ed.), Deep-seated Magmatism, Its Sources and Their Relation to Plume Processes. Glazkovskaya printing House, Irkutsk, pp. 89-107.

Wang, Y., 2012. The Mesozoic tectonism and magmatism and the destruction of the Sino-Korean Craton (North China Craton), in: (Ed.), Craton Formation and Destruction with Special Emphasis on BRICS Cratons (Abstract Volume), Univ. South Africa, Johannesburg, pp. 49-50.

Williams, J.S., 1998. U-Th-Pb geochronology by ion microprobe. Application of microanalytical techniques to understanding mineralizing processes. Rev. Econ. Geol. 7, 1-35. https://doi.org/10.5382/Rev.07.01.

Yang Q.-Y., Santosh, M., 2015. Early Cretaceous magma flare-up and its implications on gold mineralization in the Jiaodong Peninsula, China. Ore Geology Reviews 65, 626-642. https://doi.org/10.1016/j.oregeorev.2014.01.004.

Yarmolyuk, V.V., Kovalenko, V.I., Ivanov, V.G., 1995. Intraplate Late Mesozoic-Cenozoic volcanic province of central East Asia as a projection of mantle hot field. Geotektonika 5, 41-67 (in Russian).

Yarmolyuk, V.V., Kovalenko, V.I., Kuz'min, M.I., 2000. North Asian superplume activity in the Phanerozoic: magmatism and geodynamics. Geotectonics 34 (5), 343-366.

Zhai, M.G., Santosh, M., 2013. Metallogeny of the North China Craton: link with secular changes in the evolving Earth. Gondwana Res. 24, 275-297. https://doi.org/10.1016/j.gr.2013.02.007.

Captions to figures

Figure 1 Location of the Upper Amga gold district in Yakutia, and terrane map of the Aldan Stanovoy shield (a) (modified after Parfenov and Kuzmin, 2001); geological map of the Upper Amga district (b) (according to unpublished data of Yakutskgeologiya).

Figure 2 U-Pb SIMS SHRIMP-II data of the zircons from the syenite of the Upper Amga district, sample No. 16081. Zircon grains CL-images (a); U-Pb Concordia diagrams for the 16 points (b) and for the 3 diagnostic points (c) (Table 1).

Figure 3 $^{49}Ar/^{39}Ar$ age spectra for the late Mesozoic alkaline rocks of the Upper Amga district: K-feldspar (Kfs) from syenite sample No. 5088 (a), phlogopite (Phl) from lamprophyre sill sample No. 9106 (b) and K-feldspar (c) from lamprophyre dike sample No. 17086 data.

Figure 4 Photomicrographs (a, f – plane-polarized light, and d, i – with crossed nicols) and BSE images of mineral textures from the Upper Amga rocks. Here and below the abbreviations of the minerals are given according to Whitney and Evans (2010). a – d - relationships between minerals in alkaline syenites: K-feldspar (Kfs) with albite (Ab) mesoperthites and phenocrysts of K-feldspar, amphibole

(Amp), clinopyroxene (Cpx) and phlogopite (Phl) leaves. Minor and accessory minerals are apatite (Ap), magnetite (Mag), epidote (Ep), monazite-(Ce) (Mnz), chlorite (Chl) and other. K-feldspar and phlogopite matrix with the phlogopite and K-feldspar phenocrysts in the lamprophyre sills (e, f). Phenocrysts of clinopyroxene and olivine (Ol) in the lamprophyre dikes (g – i). The olivine is replaced by serpentine (Srp), the last contains the magnetite (white) grains (h). Minor and accessory minerals of the lamprophyres are apatite, magnetite, quartz (Qz), calcite (Cal) with the disseminated impregnation of pyrite (Py) (e) and other sulfide (Sul) microveinlets (f).

Figure 5 Diagrams of the Al_2O_3/FeO and Al_2O_3/TiO_2 concentration ratios of the phlogopites from the Upper Amga alkaline rocks. The trends of the alkaline rocks are based on Mitchell (1995).

Figure 6 Photomicrographs (a, c, d, e, h, i) and BSE images (b, f, g) of the mineral assemblages in the altered rocks of Upper Amga district. Pyrite (Py) with chalcopyrite (Ccp), galena (Gn) and pyrrhotite (Po) inclusions, as well as the solid solution of chalcopyrite in sphalerite (Sp) (e) in the quartz–calcite-chlorite alteration with feldspar and haematite (Hem) (a – e); Th-Ti-REE-mineralization: rutile (Rt) and monazite-(Ce) microgranular aggregates (Mnz) in quartz and later interstitial thorianite (Thrn) in the pyrite grain (f); gold–telluride mineralization represented by petzite (Ptz)–altaite (Alt)–hessite (Hes) aggregates in the pyrite grains (g); and the native gold (Au^0) mineralization forms microveins and teardrop-shaped grains in quartz.

Figure 7 Photomicrographs of the fluid inclusions (FI) in quartz of the Upper Amga gold district: (a) gas-liquid FI with a solid phase – VLS-type; (b) gas-liquid FI with liquid CO_2 phase – VLC-type; and (c) gas-liquid FI – VL-type.

Figure 8 Geological sketch showing formation of the late Mesozoic alkaline rocks and related gold mineralization within the Upper Amga district of the Aldan-Stanovoy shield.

Figure 9 Location of the mineral districts in the Chara–Aldan metallogenic province of the Aldan–Stanovoy shield, Russia (modified after Dzevanovskii et al., 1972 and Vetluzhskikh, 1990). The mineral districts associated with the late Mesozoic alkaline magmatic rocks: Upper Amga (UAR), Central Aldan (CAR), Tyrkanda (TR), Ket–Kap (KKR).

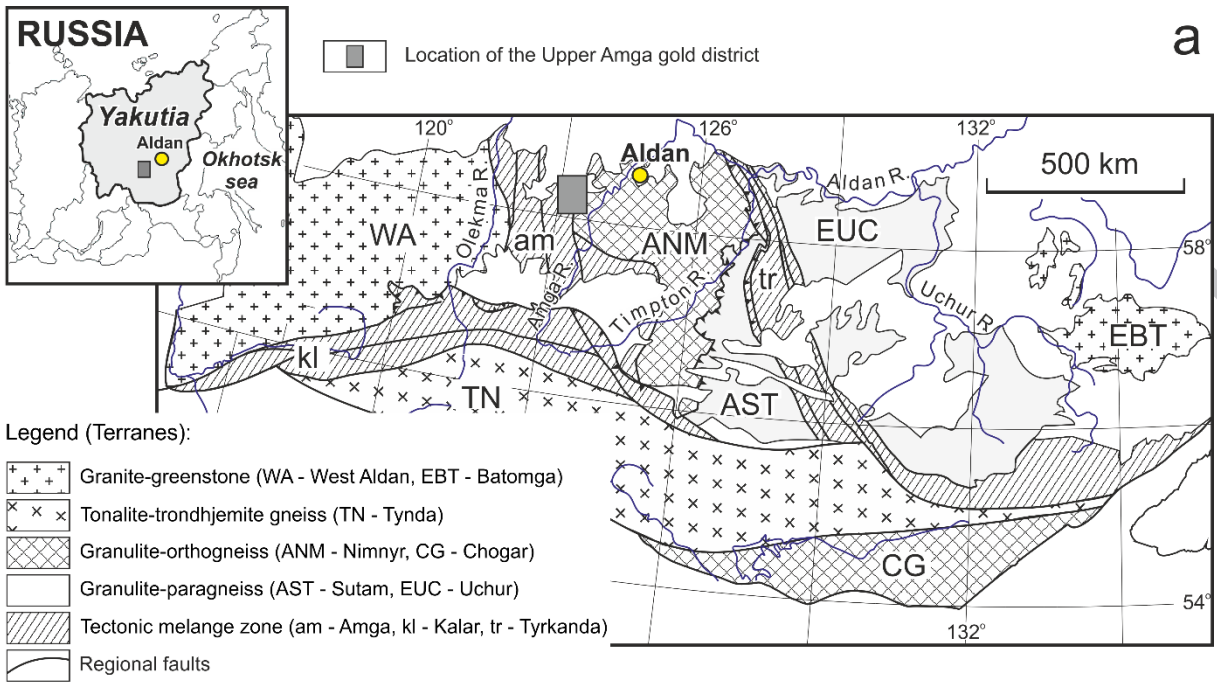

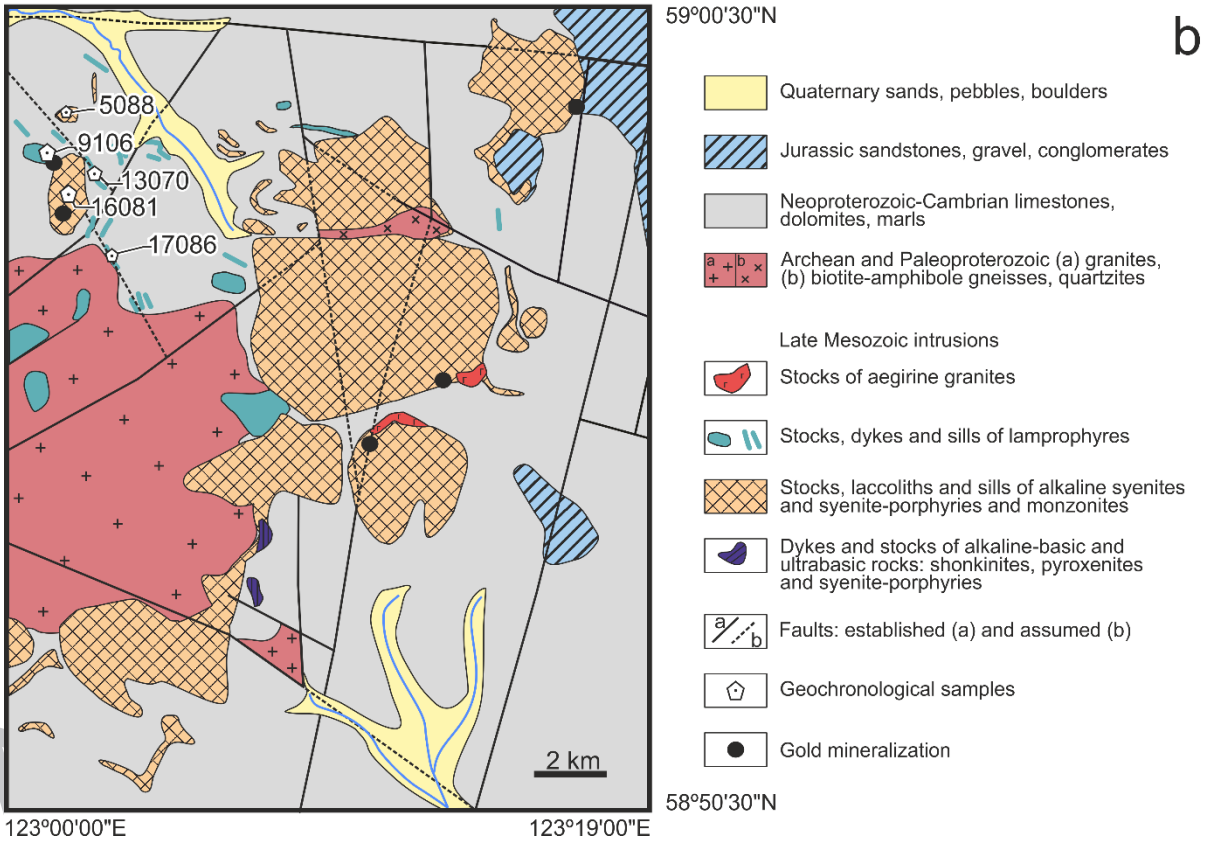

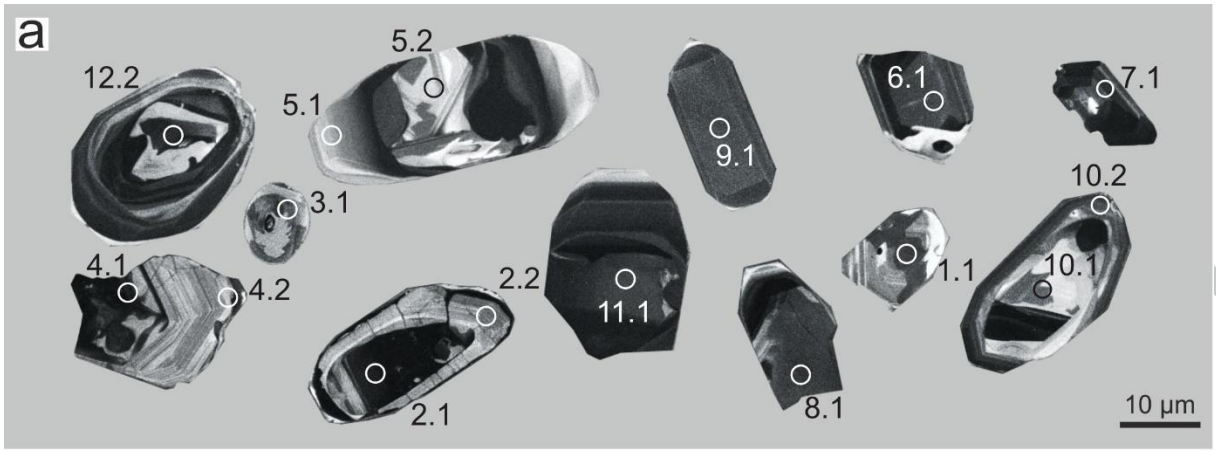

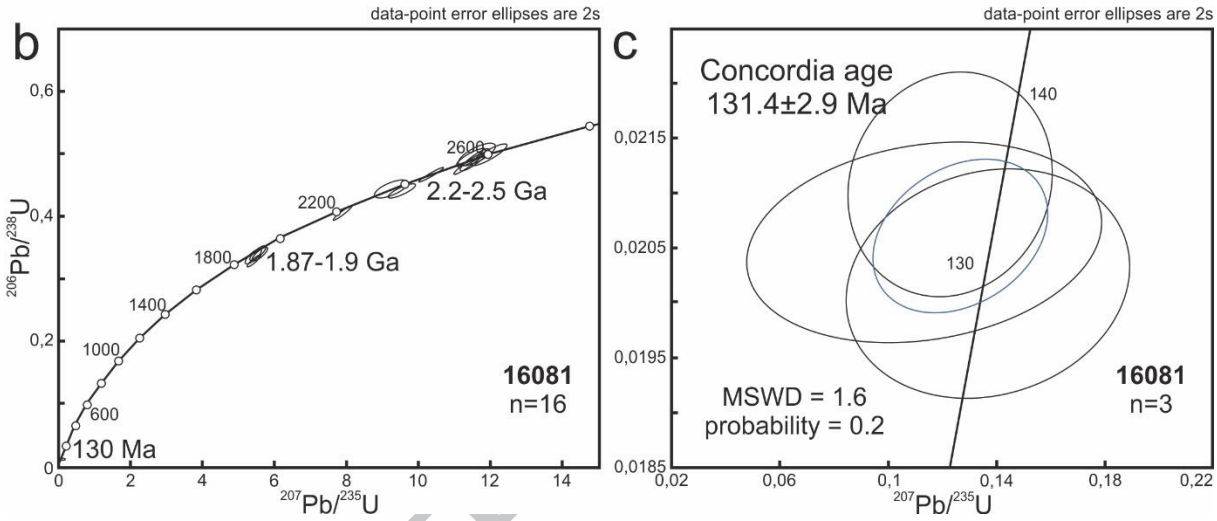

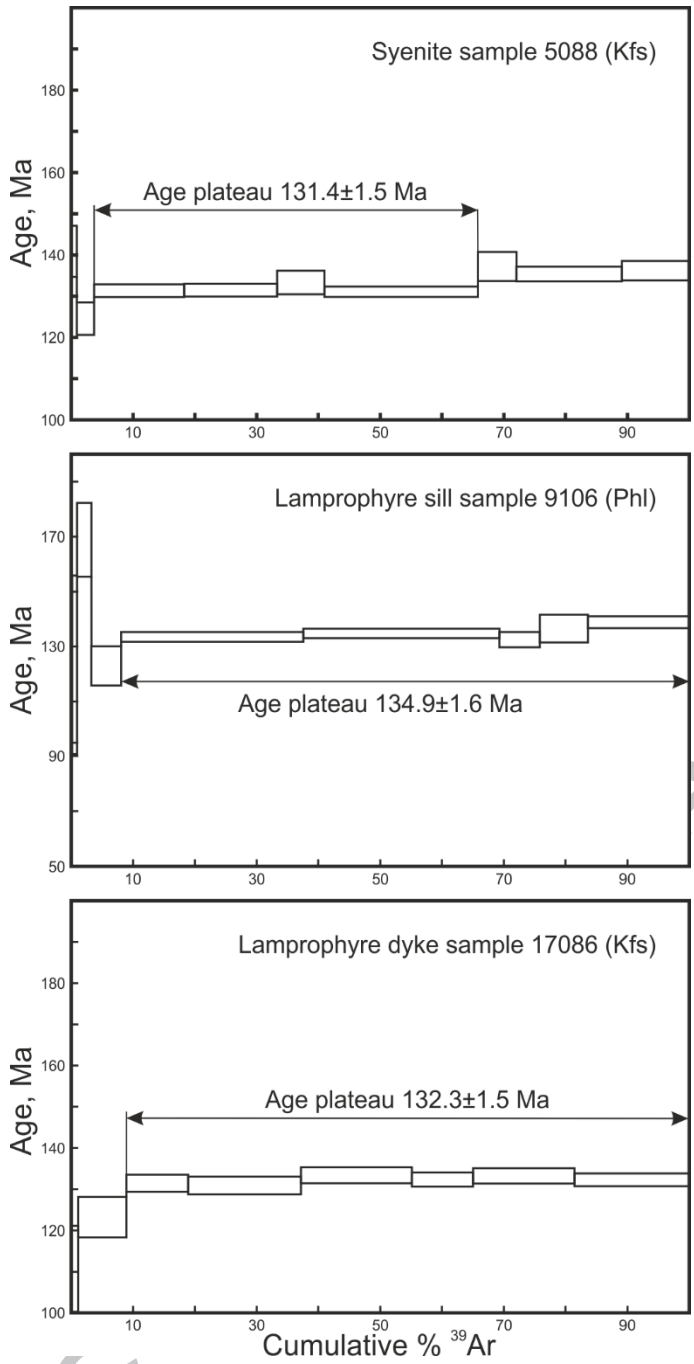

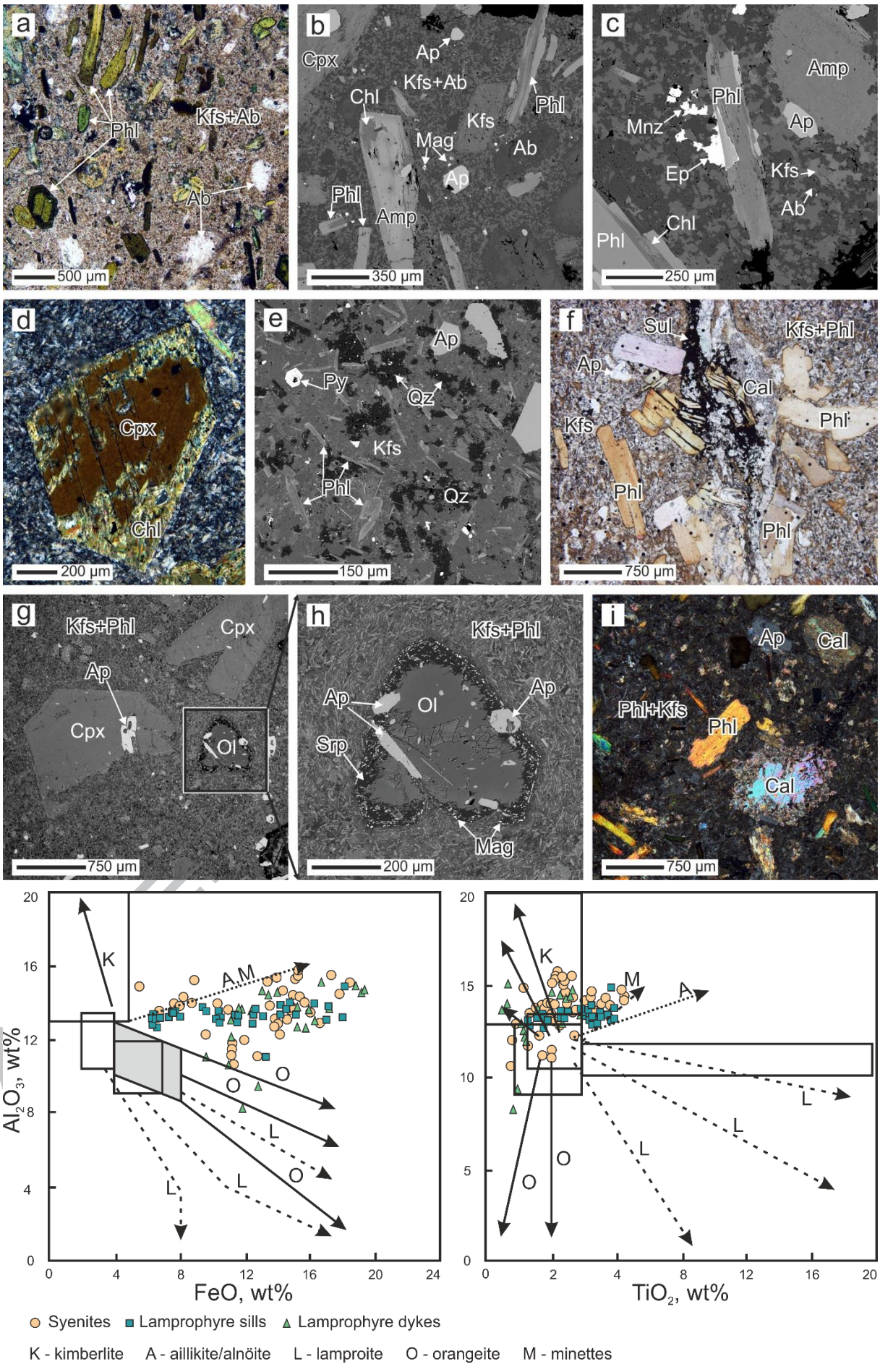
a
Phl
Kfs+Ab
Ab
500 μm
b
Cpx
Ap
Kfs+Ab
Chl
Phl
Kfs
Mag
Ab
Ap
Phl
Amp
350 μm
c
Amp
Phl
Mnz
Ap
Ep
Kfs
Ab
Chl
Phl
250 μm
d
Cpx
Chl
200 μm
e
Ap
Py
Qz
Kfs
Phl
Qz
150 μm
f
Sul
Kfs+Phl
Ap
Cal
Kfs
Phl
Phl
Phl
750 μm
g
Kfs+Phl
Cpx
Ap
Cpx
Ol
750 μm
h
Kfs+Phl
Ap
Ap
Ol
Ap
Srp
Mag
200 μm
i
Ap
Cal
Phl+Kfs
Phl
Cal
750 μm
20
16
12
8
4
0
Al_2O_3, wt%
K
A M
O
O
L
O
L
L
0
4
8
12
16
20
24
FeO, wt%
20
15
10
5
0
K
M
A
L
L
L
O
O
0
2
4
8
12
16
20
TiO_2, wt%
Syenites
Lamprophyre sills
Lamprophyre dykes
K - kimberlite
A - aillikite/alnöite
L - lamproite
O - orangeite
M - minettes

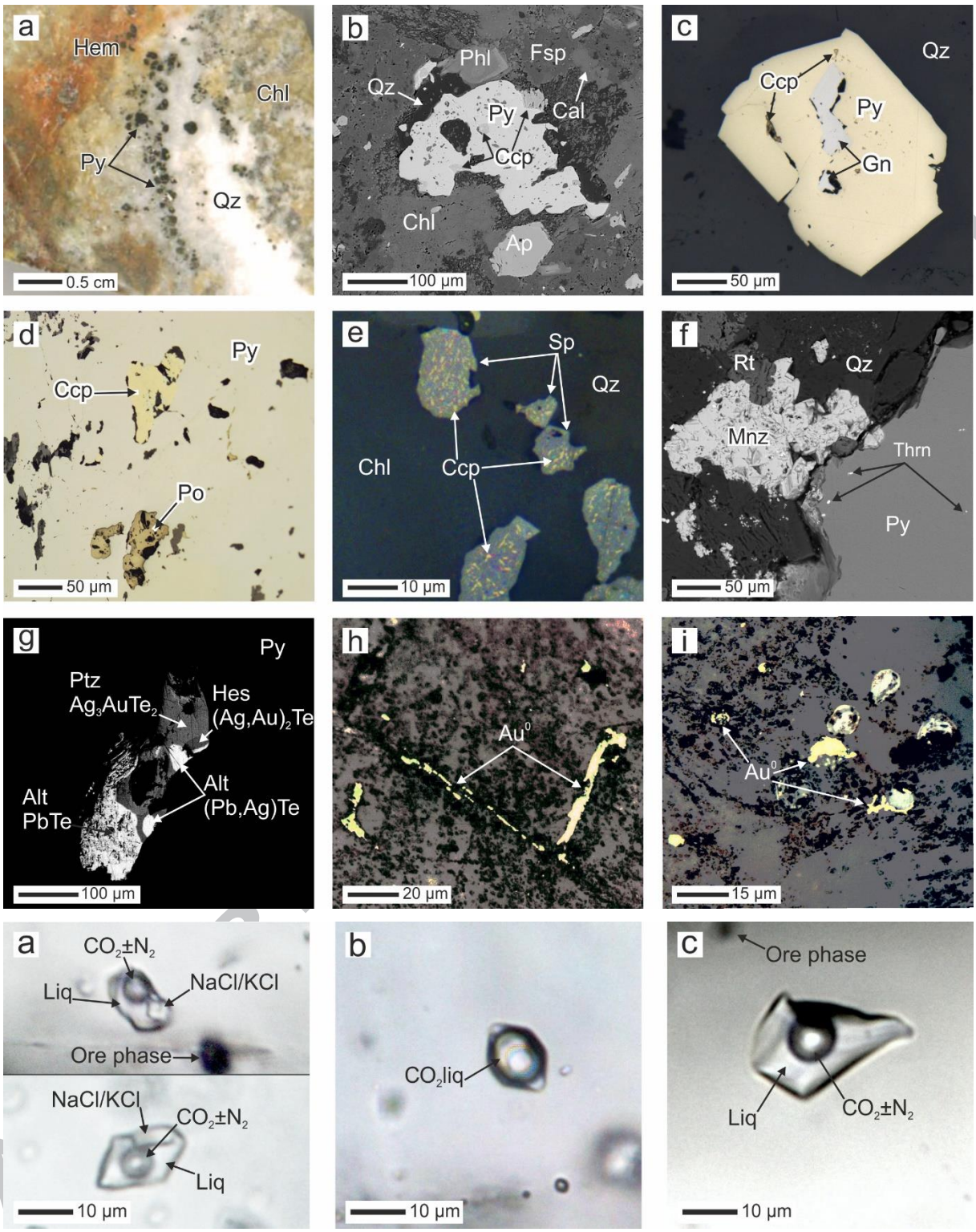
a
Hem
Chl
Py
Qz
0.5 cm
b
Phl
Fsp
Qz
Py
Cal
Ccp
Chl
Ap
100 µm
c
Qz
Ccp
Py
Gn
50 µm
d
Py
Ccp
Po
50 µm
e
Sp
Qz
Chl
Ccp
10 µm
f
Rt
Qz
Mnz
Thrn
Py
50 µm
g
Py
Ptz
Ag3AuTe2
Hes
(Ag,Au)2Te
Alt
PbTe
Alt
(Pb,Ag)Te
100 µm
h
Au0
20 µm
i
Au0
15 µm
a
CO2±N2
Liq
NaCl/KCl
Ore phase
NaCl/KCl
CO2±N2
Liq
10 µm
b
CO2liq
10 µm
c
Ore phase
Liq
CO2±N2
10 µm

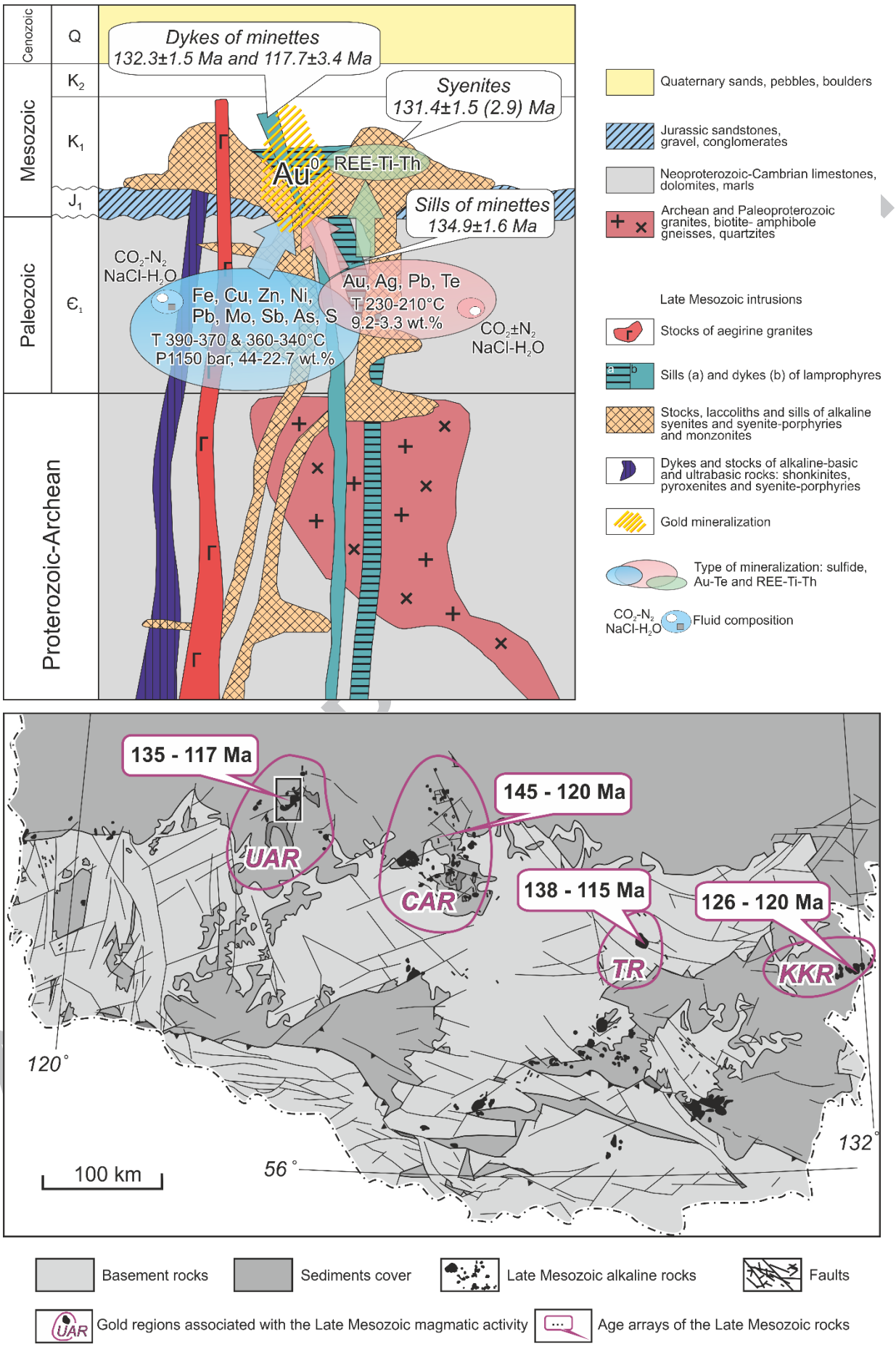

Table 1 Results of the U-Pb SIMS analysis of the zircon grains from the syenite (No. 16081) of the Upper Amga gold district

Sample/ point	% $^{206}Pb_c$	ppm U	ppm Th	$^{232}Th/^{238}U$	ppm $^{206}Pb^*$	(1) $^{206}Pb/^{238}U$ Age		(1) $^{207}Pb/^{206}Pb$ Age		% Dis-cor-dant	(1) $^{207}Pb^*/^{206}Pb^*$	± %	(1) $^{207}Pb^*/^{235}U$	± %	(1) $^{206}Pb^*/^{238}U$	± %	Err corr
16081-_1.1	0.11	198	155	0.81	85.7	2629	±30	2508	±12	-5	0.16051	0.7	11.46	1.5	0.5035	1.4	0.891
16081_2.1	0.03	737	285	0.40	263	2236	±24	2203.4	±6.9	-1	0.13809	0.4	7.9	1.3	0.4147	1.3	0.956
16081_2.2	0.12	233	93	0.41	90.2	2395	±28	2388	±13	0	0.15038	0.74	9.54	1.6	0.4585	1.4	0.885
16081_3.1	0.13	236	140	0.61	71.1	1937	±24	1876	±19	-3	0.11547	1	5.543	1.8	0.3504	1.4	0.804
16081_4.1	0.11	686	47	0.07	199	1876	±21	1905	±10	2	0.11661	0.58	5.431	1.4	0.3378	1.3	0.911
16081_4.2	0.01	163	69	0.44	63.4	2410	±28	2322	±23	-4	0.14079	1.4	9.24	2	0.4532	1.4	0.716
16081_5.1	0.07	219	66	0.31	65.6	1929	±23	1901	±17	-1	0.11664	0.96	5.595	1.7	0.3487	1.4	0.818
16081_5.2	0.10	108	44	0.43	47	2650	±32	2516	±20	-5	0.16058	1.2	11.63	1.9	0.5084	1.5	0.771
16081_6.1	0.64	213	97	0.47	3.88	13 ± 4.5	2.6			-274	0.04 19	13	0.122	13	0.02 108	2	0.153
16081_7.1	1.14	575	591	1.06	10.2	13 ± 1	2.4			-362	0.04 01	23	0.114	23	0.02 053	1.9	0.079
16081_8.1	0.09	316	152	0.50	136	2613	±29	2536	±10	-3	0.16078	0.61	11.56	1.5	0.4997	1.3	0.909
16081_9.1	0.14	288	168	0.60	85.4	1911	±23	1861	±19	-3	0.11538	1.1	5.415	1.7	0.3452	1.4	0.793
16081_10.1	0.07	107	55	0.53	46.7	2648	±34	2566	±14	-3	0.17008	0.86	11.96	1.8	0.5079	1.5	0.873
16081_10.2	0.92	184	109	0.61	3.23	129 ± 9	2.6			12	0.04 89	16	0.136	16	0.02 021	2	0.129
16081_11.1	0.01	433	239	0.57	183	2586	±28	2532.4	±7	-2	0.16745	0.42	11.39	1.4	0.4935	1.3	0.952
16081_12.1	0.02	589	442	0.77	241	2510	±27	2432.1	±6.7	-3	0.15779	0.4	10.36	1.4	0.476	1.3	0.956

Note: errors are 1-sigma; Pbc and Pb* indicate the common and radiogenic portions, respectively. Error in Standard calibration was 0.51% (not included in above errors but required when comparing data from different mounts). (1) Common Pb corrected using measured ^{204}Pb.

Table 2
Results of Ar-Ar dating of the K-feldspar from the syenite sample No. 5088 of the Upper Amga district

T, ^0C	$^{40}Ar/^{39}Ar$	±	$^{38}Ar/^{39}Ar$	±	$^{37}Ar/^{39}Ar$	±	$^{36}Ar/^{39}Ar$	±	^{39}Ar, % cumu-lative	Age, (Ma)	±
500	79.2	0.3	0.05	0.01	0.10	0.05	0.191	0.003	0.8	140.9	6.2

600	39.23	0.08	0.028	0.001	0.07	0.01	0.065	0.002	3.7	124.5	3.8
700	24.90	0.02	0.018	0.001	0.159	0.004	0.0129	0.0006	18.3	131.3	1.6
775	24.56	0.01	0.0173	0.0004	0.48	0.01	0.0117	0.0005	33.4	131.4	1.5
840	25.51	0.05	0.016	0.001	0.73	0.02	0.014	0.002	41.0	133.2	2.9
930	22.792	0.007	0.0172	0.0004	0.057	0.002	0.0058	0.0002	65.8	131.1	1.3
980	25.01	0.05	0.0136	0.0004	0.02	0.01	0.010	0.002	72.0	137.2	3.6
1050	23.52	0.02	0.0123	0.0006	0.021	0.004	0.0059	0.0007	89.2	135.3	1.7
1130	25.06	0.03	0.0191	0.0002	0.004	0.004	0.011	0.001	100.0	136.2	2.4

Table 3

Results of Ar-Ar dating of the phlogopite from the lamprophyre sill sample No. 9106 of the Upper Amga district

T, ^{0}C	^{40}Ar/^{39}Ar	±	^{38}Ar/^{39}Ar	±	^{37}Ar/^{39}Ar	±	^{36}Ar/^{39}Ar	±	^{39}Ar, % cumu-lative	Age, (Ma)	±
500	64.7	1.1	0.09	0.01	0.01	0.01	0.15	0.02	0.9	123.4	32.4
610	40.1	0.3	0.03	0.01	0.19	0.03	0.045	0.007	3.2	168.7	13.4
720	32.4	0.1	0.038	0.005	0.44	0.03	0.045	0.004	8.0	122.8	7.1
830	24.02	0.02	0.02	0.0005	0.0398	0.0008	0.0105	0.0006	37.5	133.4	1.7
890	22.1	0.02	0.0142	0.0004	0.020	0.004	0.0033	0.0006	69.3	134.8	1.7
950	26.39	0.04	0.019	0.003	0.05	0.03	0.019	0.001	75.8	132.4	2.7
1030	26.43	0.07	0.016	0.002	0.018	0.007	0.017	0.003	83.8	136.5	5.1
1130	24.08	0.02	0.0221	0.0009	0.014	0.003	0.0077	0.0010	100.0	138.8	2.2

Table 4

Results of Ar-Ar dating of the K-feldspar from the lamprophyre dyke sample No 17086 of the Upper Amga district

T, ^{0}C	^{40}Ar/^{39}Ar	±	^{38}Ar/^{39}Ar	±	^{37}Ar/^{39}Ar	±	^{36}Ar/^{39}Ar	±	^{39}Ar, % cumu-lative	Age, (Ma)	±
500	45.2	1.1	0.048	0.004	0.12	0.03	0.10	0.01	1.1	97.3	23.9
620	25.5	0.2	0.0178	0.0006	0.153	0.007	0.020	0.003	8.9	123.2	4.8
720	23.65	0.02	0.0169	0.0007	0.539	0.010	0.0093	0.0009	19.0	131.4	2.0
810	23.41	0.03	0.0166	0.0007	0.189	0.003	0.0088	0.0009	37.2	131.0	2.0
880	22.97	0.02	0.0171	0.0002	0.031	0.002	0.0060	0.0009	55.1	133.3	2.0
950	23.93	0.02	0.0174	0.0006	0.031	0.005	0.0098	0.0006	64.9	132.4	1.7
1040	23.89	0.02	0.0169	0.0005	0.047	0.004	0.0091	0.0008	81.3	133.3	1.9
1130	23.81	0.02	0.0167	0.0006	0.035	0.003	0.0094	0.0005	100.0	132.3	1.5

Table 5
Representative electron-microprobe analyses of phlogopite from the Upper Amga alkaline magmatic rocks, wt.%

	Syenites					Lamprophyre sills					Lamprophyre dykes				
SiO_2	45.08	43.96	39.28	39.77	37.42	38.30	36.24	36.50	38.21	37.46	37.99	39.79	36.26	38.25	37.99
TiO_2	2.14	2.12	2.25	1.65	2.40	3.22	3.84	3.77	3.25	3.05	0.72	1.17	2.69	2.47	0.72
Al_2O_3	15.17	13.09	12.83	12.26	15.49	14.02	14.93	13.98	13.42	13.40	15.10	12.58	14.79	14.34	15.10
Cr_2O_3	0.00	0.00	0.00	0.00	0.00	0.00	0.00	0.00	0.00	0.00	0.32	0.00	0.00	0.00	0.32
FeOt*	13.41	13.83	13.83	12.70	17.37	13.82	18.14	16.24	12.53	14.19	16.78	15.81	19.00	13.51	16.78
MnO	0.00	0.00	0.00	0.00	0.00	0.00	0.00	0.00	0.00	0.00	0.00	0.00	0.00	0.00	0.00
MgO	13.03	15.97	17.33	15.82	14.03	17.30	13.42	15.22	18.69	17.06	15.21	16.50	13.02	16.37	15.21
CaO	0.00	0.00	1.46	3.75	0.00	0.00	0.00	0.00	0.00	0.00	0.15	0.00	0.87	0.00	0.15
Na_2O	0.00	0.00	0.00	0.00	0.00	0.00	0.00	0.00	0.18	0.00	0.00	0.00	0.00	0.65	0.00
K_2O	9.85	9.77	9.55	9.72	9.23	9.55	9.12	8.95	9.08	9.49	9.75	9.60	9.13	9.17	9.75
BaO	0.00	0.00	0.00	0.00	0.00	0.96	1.34	1.38	1.19	1.38	0.00	0.00	1.59	1.44	0.00
Cl	0.15	0.00	0.00	0.19	0.39	0.00	0.17	0.00	0.00	0.00	0.00	0.00	0.00	0.00	0.00
Total	98.83	98.74	96.53	95.86	96.33	97.17	97.20	96.04	96.55	96.03	96.02	95.45	97.35	96.20	96.02
Si	3.14	3.10	2.85	2.86	2.80	2.83	2.73	2.75	2.81	2.80	2.84	2.97	2.72	2.84	2.84
Ti	0.11	0.11	0.12	0.09	0.14	0.17	0.22	0.21	0.18	0.17	0.04	0.07	0.15	0.14	0.04
Al	1.25	1.09	1.10	1.04	1.37	1.19	1.32	1.24	1.16	1.18	1.33	1.11	1.31	1.25	1.33
Cr	0.00	0.00	0.00	0.00	0.00	0.00	0.00	0.00	0.00	0.00	0.02	0.00	0.00	0.00	0.02
Fe	0.78	0.82	0.84	0.58	1.09	0.89	1.14	1.02	0.77	0.89	1.05	0.99	1.19	0.84	1.05
Mn	0.00	0.00	0.00	0.00	0.00	0.00	0.00	0.00	0.00	0.00	0.00	0.00	0.00	0.00	0.00
Mg	1.36	1.68	1.88	1.69	1.56	1.86	1.51	1.71	2.05	1.90	1.69	1.83	1.46	1.81	1.69
Ca	0.00	0.00	0.11	0.29	0.00	0.00	0.00	0.00	0.00	0.00	0.01	0.00	0.07	0.00	0.01
Na	0.00	0.00	0.00	0.00	0.00	0.00	0.00	0.00	0.03	0.00	0.00	0.00	0.00	0.09	0.00
K	0.88	0.88	0.88	0.89	0.88	0.88	0.88	0.86	0.85	0.91	0.93	0.91	0.87	0.87	0.93
Ba	0.00	0.00	0.00	0.00	0.00	0.03	0.04	0.04	0.03	0.04	0.00	0.00	0.05	0.04	0.00
Cl	0.02	0.00	0.00	0.02	0.05	0.00	0.00	0.00	0.00	0.00	0.00	0.00	0.00	0.00	0.00
OH	1.98	2.00	2.00	1.98	1.95	2.00	2.00	2.00	2.00	2.00	2.00	2.00	2.00	2.00	2.00

Note: *here and below: FeOt = total iron; 0.00= below detection limit.

Table 6

Representative electron-microprobe analyses of amphibole and clinopyroxene from the Upper Amga alkaline rocks, wt.%

Amphibole									
	Syenites				Lamprophyres				
SiO_2	55.3	55.77	39.54	55.28	45.57	42.68	51.49	46.42	55.32
TiO_2	0.00	0.00	1.72	0.00	0.78	1.18	0.00	0.82	0.00
Al_2O_3	1.61	2.06	12.68	1.53	10.75	13.15	4.91	9.05	1.19
MnO	0.26	0.00	0.43	0.00	0.00	0.00	0.41	0.44	0.00
FeO	8.92	8.97	20.12	11.78	13.5	14.9	11.48	12.3	9.08
MgO	18.92	19.05	7.45	16.83	13.96	12.3	17.05	14.76	18.39
CaO	11.24	12.86	11.01	12.27	11.18	10.96	10.63	11.33	12.72
Na_2O	0.2	0.46	2.17	0.38	1.85	2.25	1.01	1.46	0.00
K_2O	0.31	0.18	2.00	0.11	0.93	0.86	0.24	0.78	0.00
Cl	0.00	0.00	0.00	0.00	0.3	0.62	0.17	0.24	0.00
Total	96.76	99.35	97.12	98.18	98.82	98.9	97.39	97.6	96.7
Formulae based on 24 atoms of oxygen, apfu									
Si	7.862	7.729	6.147	7.844	6.6	6.238	7.355	6.735	7.876
Al	0.27	0.337	2.323	0.256	1.835	2.265	0.826	1.548	0.2
Ti	0.000	0.000	0.201	0.000	0.085	0.13	0.000	0.09	0.000
Fe3+	0.003	0.146	0.123	0.085	0.295	0.504	0.42	0.501	0.049
Fe2+	1.057	0.894	2.493	1.313	1.34	1.317	0.951	0.992	1.033
Mg	4.01	3.936	1.727	3.56	3.014	2.68	3.631	3.193	3.903
Mn	0.031	0.000	0.057	0.000	0.000	0.000	0.05	0.054	0.000
Ca	1.712	1.91	1.834	1.865	1.735	1.716	1.627	1.761	1.94
Na	0.055	0.124	0.654	0.105	0.52	0.638	0.28	0.411	0.000
K	0.056	0.032	0.397	0.02	0.172	0.16	0.044	0.144	0.000
OH	2	2	2	2	1.926	1.846	1.959	1.941	2
Cl	0.000	0.000	0.000	0.000	0.074	0.154	0.041	0.059	0.000
Minerals	Act	Act	Fprg	Act	Prg	Mhs	Mfhbl	Mfhbl	Act

Clinopyroxene						
	Syenites		Lamprophyre dykes			
SiO_2	56.91	56.48	50.42	51.52	51.64	53.08
TiO_2	0.00	0.00	0.78	0.5	0.55	0.42
Al_2O_3	1.59	1.44	4.08	2.87	2.82	2.06
Cr_2O_3	0.00	0.00	0.00	0.22	0.66	0.75
FeO	12.62	12.71	7.18	4.85	4.53	3.95
MgO	17.26	16.45	14.34	15.39	15.37	16.52
CaO	12.62	12.65	23.06	23.49	23.55	23.42
Na_2O	0.00	0.36	0.47	0.24	0.00	0.18
Total	101.00	100.09	100.33	99.08	99.12	100.38
Formulae based on 6 atoms of oxygen, apfu						
Si	2.000	2.000	1.853	1.907	1.916	1.934
Ti	0.000	0.000	0.022	0.014	0.015	0.012
Al	0.069	0.063	0.177	0.125	0.123	0.088
Fe3+	0.000	0.000	0.107	0.044	0.000	0.012
Cr3+	0.000	0.000	0.000	0.006	0.019	0.022
Fe2+	0.389	0.395	0.114	0.106	0.141	0.108
Mg	0.948	0.912	0.786	0.849	0.850	0.897
Ca	0.498	0.504	0.908	0.931	0.936	0.914
Na	0.000	0.026	0.033	0.017	0.000	0.013
Minals						
Aeg	0.0	0.0	2.9	1.6	0.0	1.1
Fts	0.0	0.0	3.2	1.2	0.0	0.0
Jd	0.0	2.6	2.9	1.6	0.0	0.1
Ti-Aeg	0.0	0.0	0.0	0.0	0.0	0.0
Ti-Ts	0.0	0.0	1.9	1.3	1.4	1.1
Al-Ts	7.0	6.3	15.3	11.3	11.3	7.3
Di	35.8	35.3	61.3	71.4	72.2	76.3
Hd	14.7	15.3	8.9	8.9	11.9	9.2
En	30.1	28.2	3.3	2.6	2.7	4.4
Fs	12.4	12.2	0.5	0.3	0.5	0.5

Abbreviations: Act – actinolite, Fprg – ferro-pargasite, Prg – pargasite, Mhs – magnesio-hastingsite, Mfhbl – magnesio-ferro-hornblende, Aeg – aegirine, Fts – ferro-tschermakite, Jd – jadeite, Ts – tschermakite, Di – diopside, Hd – hedenbergite, En – enstatite, Fs – ferrosilite.

Table 7 Results of fluid inclusion study of the quartz from the Upper Amga district

Host mineral	Ore assemblage	Type of FI	Th, °C	Tm, °C	Concentration, wt. % NaCl-equ.	Gas phase	P, bar
Qu-1	Py	P VLS	370-390	---	42-44	CO_2-N_2	---
	Ccp, Po, Gn, Sp…	PS VL	330-350	-20…-10	14-22.7		
Qu-2	Qu	P VLC	340-360	---	---	CO_2 liq	1150
	Ptz, Hes, Alt, Au^0	PS VL	210-230	-6…-2	3.3-9.2	$CO_2 \pm N_2$	---

Note: the description of the host minerals and the types of the fluid inclusion (FI) are in the text of the section; P – primary, PS – pseudo-secondary FI; the parameters of interpretation is in the Analytical methods section; abbreviation of the ore-minerals are in the section Gold mineralisation.

5. The magmatic rocks of the Upper Amga ore district are represented by syenites and lamprophyres. The age of syenites is 131.4 ± 1.5 (2.9) Ma; and the lamprophyres were formed during the intervals of 134.9 ± 1.6 – 132.3 ± 1.5 and 117.7 ± 3.4 Ma.
6. Three types of mineralization are presented by the REE-Ti-Th, sulfides and telluride-gold ores.